Stem Cell Reports
Article
ISSCR
OPEN ACCESS

Human Cortical Organoids Expose a Differential Function of GSK3 on Cortical Neurogenesis

Alejandro López-Tobón,[1,2,8] Carlo Emanuele Villa,[1,8] Cristina Cheroni,[1,2,8] Sebastiano Trattaro,[1,2] Nicolò Caporale,[1,2] Paola Conforti,[3,4] Raffaele Iennaco,[3,4] Maria Lachgar,[5,9,10] Marco Tullio Rigoli,[1] Berta Marcó de la Cruz,[1] Pietro Lo Riso,[1] Erika Tenderini,[1] Flavia Troglio,[1] Marco De Simone,[4,6] Isabel Liste-Noya,[5] Giuseppe Macino,[7] Massimiliano Pagani,[4,6] Elena Cattaneo,[3,4] and Giuseppe Testa[1,2,*]
[1]Laboratory of Stem Cell Epigenetics, IEO, European Institute of Oncology, IRCCS, Milan, Italy
[2]Department of Oncology and Hemato-oncology, University of Milan, Milan, Italy
[3]Department of Biosciences, University of Milan, Milan 20133, Italy
[4]Istituto Nazionale di Genetica Molecolare "Romeo ed Enrica Invernizzi", Milan 20122, Italy
[5]Unidad de Regeneración Neural, Unidad Funcional de Investigación de Enfermedades Crónicas, Instituto de Salud Carlos III (ISCIII), Madrid, Spain
[6]Department of Medical Biotechnology and Translational Medicine, University of Milan, Milan, Italy
[7]Department of Molecular Medicine, Sapienza Università di Roma, Rome, Italy
[8]Co-first author
[9]Present address: Servicio de Genética, Instituto Ramón y Cajal de Investigación Sanitaria, Hospital Universitario Ramón y Cajal, Madrid, Spain
[10]Present address: Center for Biomedical Network Research on Rare Diseases, Instituto de Salud Carlos III, Madrid, Spain
*Correspondence: giuseppe.testa@ieo.it
https://doi.org/10.1016/j.stemcr.2019.09.005

SUMMARY

The regulation of the proliferation and polarity of neural progenitors is crucial for the development of the brain cortex. Animal studies have implicated glycogen synthase kinase 3 (GSK3) as a pivotal regulator of both proliferation and polarity, yet the functional relevance of its signaling for the unique features of human corticogenesis remains to be elucidated. We harnessed human cortical brain organoids to probe the longitudinal impact of GSK3 inhibition through multiple developmental stages. Chronic GSK3 inhibition increased the proliferation of neural progenitors and caused massive derangement of cortical tissue architecture. Single-cell transcriptome profiling revealed a direct impact on early neurogenesis and uncovered a selective role of GSK3 in the regulation of glutamatergic lineages and outer radial glia output. Our dissection of the GSK3-dependent transcriptional network in human corticogenesis underscores the robustness of the programs determining neuronal identity independent of tissue architecture.

INTRODUCTION

Neurogenesis is initiated by the formation of a neuroepithelium, composed of neural stem cells (NSCs) organized in apico-basal orientation that divide symmetrically leading to a rapid expansion of the NSC pool (Taverna et al., 2014). The polarization of the neuroepithelium precedes the differentiation of NSCs into radial glia cells (RGCs), and triggers the elongation of cytoplasmic processes that form a migratory scaffold for newborn neurons (Betizeau et al., 2013). Such polarization is in turn necessary for the acquisition of the key properties that define tissue organization (Johansson et al., 2010).

Glycogen synthase kinase 3 alpha and beta (GSK3α and β) are serine/threonine kinases encoded by two different genes, which function as integrating hubs for multiple proliferation and differentiation signals due to their central role in the receptor tyrosine kinase, Wnt and sonic hedgehog signaling pathways (Kim et al., 2009; McCubrey et al., 2016). GSK3 is involved in neurodevelopment through the phosphorylation of a broad set of substrates, including transcription factors essential for brain development, such as CREB (Grimes and Jope, 2001a), neurogenin2 (Ma et al., 2008), β-catenin (Aberle et al., 1997), and multiple microtubule-associated proteins (Fumoto et al., 2008; Hur and Zhou, 2010). Studies in animal models have provided a wealth of evidence linking GSK3 activity to the regulation of early and late neurogenesis in a stage-wise fashion. Its activity is required to maintain the overall polarity of the radial glia scaffold (Yokota et al., 2010). Genetic ablation of both *GSK3α* and *GSK3β* in RGCs results in a massive increase in neural progenitor proliferation, with marked suppression of intermediate progenitor cells (IPCs) and postmitotic neurons (Kim et al., 2009). However, paralog-specific knockdown at later stages results in distinct outcomes, with the loss of *GSK3β* markedly decreasing the production of IPCs and upper-layer Cux1-positive neurons (Ma et al., 2017).

Despite the abundant evidence connecting GSK3 to neurogenesis in various animal models, much less is known of its role in the far more complex human context, mostly due to the lack of models that efficiently recapitulate the human-specific range of progenitor subpopulations. Seminal work conducted in human embryonic stem cells (hESCs) demonstrated their proficiency to form 3D aggregates containing self-organized apico-basally polarized cortical tissues with neurogenic properties (Watanabe et al., 2005). These 3D aggregates are able to generate features usually

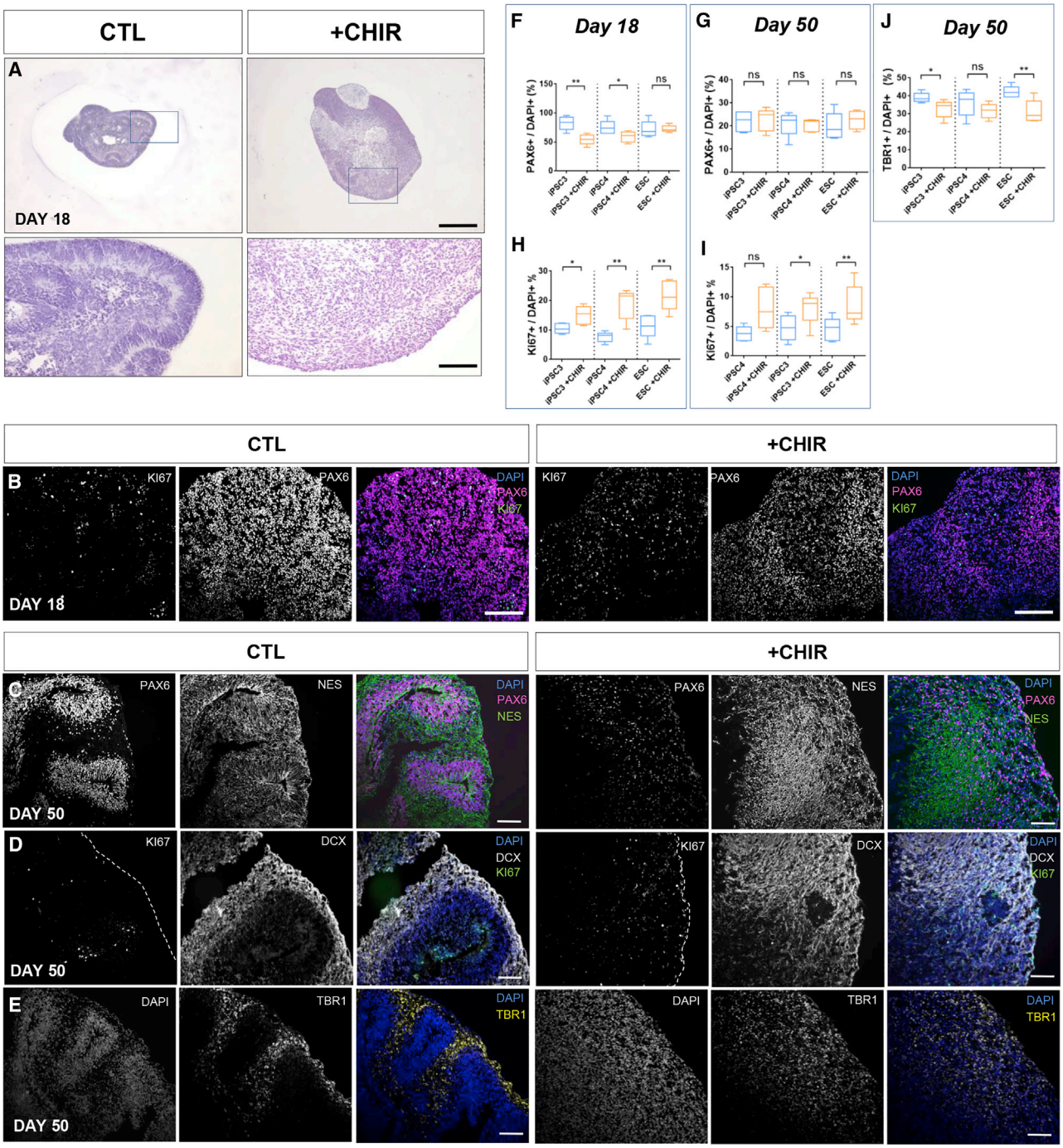

Figure 1. Morphogenetic Alterations Caused by Chronic GSK3 Inhibition

(A) Representative captions of cortical organoids at day 18, stained with H&E (magnifications: upper, 10×; lower, 63×). Scale bars, 200 and 10 μm, respectively.

(B) Representative images from day 18 organoids immunostained with anti-PAX6 (red), anti-KI67 (green), and DAPI (blue), wide-field fluorescence images. Scale bar, 50 μm.

(C–E) Representative images from day 50 organoids immunostained with: (C) anti-PAX6 (red), anti-Nestin (green), and DAPI (blue), (D) anti-DCX (white), anti-KI67 (green), and DAPI (blue), and (E) anti-TBR1 (yellow) and DAPI (blue). Scale bars, 50 μm.

(legend continued on next page)

absent in monolayer cultures, such as specific progenitor subpopulations and organizing centers (Eiraku et al., 2008; Kadoshima et al., 2013), constituting the precursors of current brain organoids protocols. Brain organoids have emerged as the most promising alternative to model neurodevelopment under a strictly human genetic background (Di Lullo and Kriegstein, 2017). Their ontogeny recapitulates most of the salient features of early to mid-fetal brain development, including progenitor populations and distribution of cell domains (Lancaster et al., 2013; Mariani et al., 2015, 2012; Paşca et al., 2015). Single-cell transcriptional profiling of organoids revealed a cellular diversity that closely matches in composition and transcriptional landscape the human fetal brain and confirmed the presence of human progenitor populations responsible for neocortical expansion (Amiri et al., 2018; Camp et al., 2015; Quadrato et al., 2017).

Here we explore the role of GSK3 on early to middle corticogenesis through the chronic and specific inhibition of its activity in human cortical organoids. By combining morphological characterization with massive parallel RNA sequencing (RNA-seq) on bulk and single cells, we uncover the molecular pathways modulated by GSK3 and break down its effect on distinct cell subpopulations of the developing human cortex, revealing a differential impact on neuronal progenitor subtypes and outer radial glia (oRG) output.

RESULTS

GSK3 Is Essential for Cortical Organoid Morphogenesis

Patterned cortical organoids follow a stereotypical morphogenesis beginning with RGCs aligned in three dimensions around ventricle-like structures (VLS), mimicking the hierarchical organization of the ventricular zone of the dorsal telencephalon. Polarized RGCs are evident by day 18 (Figure 1A), with NESTIN+/PAX6+ cells comprising about 80% of the population (Figure 1B). This proportion decreases over time and becomes restricted to well-confined proliferative domains that gradually generate the neurons of the cortical plate (Paşca et al., 2015). To investigate the role of GSK3 activity throughout corticogenesis, we chronically exposed cortical organoids to the most specific GSK3 inhibitor available CHIR99021 (termed CHIR hereafter) at a 1 μM concentration, selected below the threshold for endodermal or mesodermal lineage induction in hPSCs (Patsch et al., 2015). Chronic GSK3 inhibition resulted in an increase in organoid size (Figures 1A and 2F) concomitant with a virtually complete loss of VLS (Figures 1A and 1B), with a stronger effect by day 50 (Figures 1C–1E). Unexpectedly, this difference in organoid size and radial organization was accompanied by a marginal decrease of PAX6+ cells at day 18 (Figure 1F) (CTL 76 ± 3.3, CHIR 65 ± 2.7), as well as of its expression levels (Figure S1A), while no significant difference was observed at day 50 in the proportion of PAX6+ cells (Figure 1G) (CTL 20 ± 1.2, CHIR 22 ± 1.0). Moreover, staining of early neuron markers TBR1 (layer V–VI neuronal progenitors) (Figure 1E) and DCX (Figure 1D) revealed a profound disarray in tissue architecture with only a slight reduction in TBR1+ cells (CTL 39 ± 1.3, CHIR 32 ± 1.3) (Figure 1J), indicating that GSK3 activity is critical for the correct morphogenesis of the developing cortex.

To dissect the mechanisms underlying this morphogenic defect, we adopted a two-tiered strategy: (1) a validation in a classic 2D model attuned to quantify essential properties of NSCs such as polarity and proliferation (Conforti et al., 2018); and (2) transcriptional profiling of patterned cortical organoids at 18, 50 and 100 days for a dynamic characterization of early corticogenesis (Figure 2A). We followed the emergence of 2D neural rosettes until 20 days *in vitro*, when rosettes are typically PASL1+ at the apical end. GSK3 inhibition drastically reduced rosette number (Figures 2B and 2C) as well as the average size of formed rosette lumens (Figure 2D). Likewise, a growth curve for 72 h revealed an increase in proliferation rate up to 1.5-fold compared with control (Figure 2E), indicating that both the morphogenic disarray and the increased size observed in early cortical organoids arise from aberrations already present during the transition from pluripotency to NSCs. In addition, we quantified the impact of GSK3 inhibition on organoid size through a growth measurement over a 40-day time course. We found a sustained increase in organoid size upon chronic GSK3 inhibition (Figures 2F–2H), with a robust surge in pace between days 10 and 15, subsequent to the time point when cortical organoids begin to be exposed to proliferation-boosting factors, fibroblast growth factor 2 and epidermal growth factor (Figure 2H), in agreement with the increased proliferation rate observed at the first 72 h of neural induction (Figure 2E) and pointing to a growth factor-mediated proliferation process.

A previous report suggested that the sustained application of CHIR99021 in forebrain organoids after day 12 of differentiation decreased the number of Caspase 3+ core

(F and G) Quantification of the proportion of PAX6+ nuclei relative to total nuclei (DAPI) at (F) day 18 and (G) day 50 of differentiation. (H and I) Quantification of the proportion of KI67+ nuclei relative to total nuclei (DAPI) at (H) day 18 and (I) day 50 of differentiation. (J) Quantification of the proportion of TBR1+ nuclei relative to total nuclei (DAPI) in day 50 organoids. All quantifications were performed in five organoids per line, three independent hPSC lines (N = 15, n = 3), unpaired t test; *p < 0.05, **p < 0.01, ***p < 0.001.

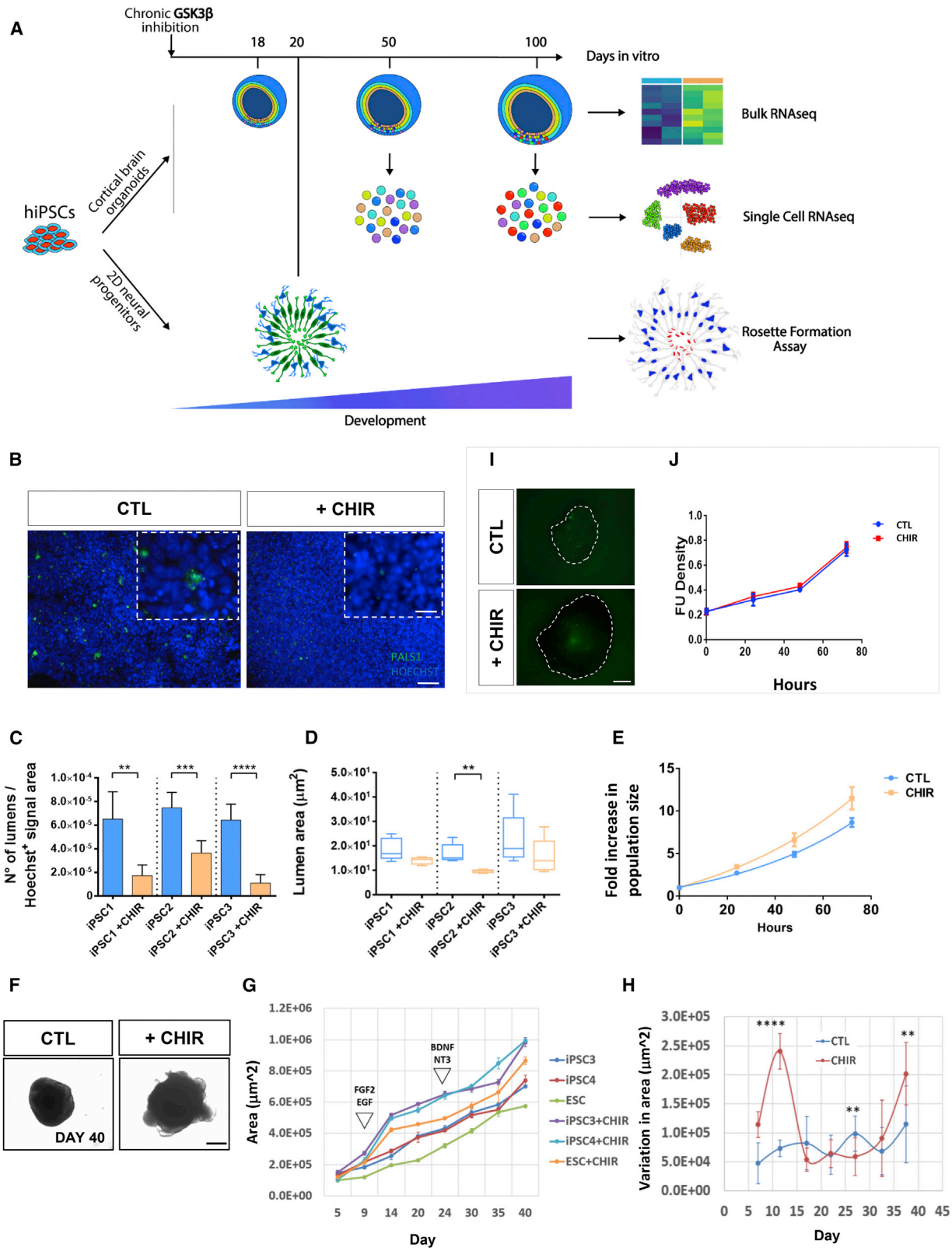

(legend on next page)

cells (Qian et al., 2016), which could explain the increase in organoid size. To test whether chronic CHIR application had an overall effect on cell viability, we performed luminescent quantitation of membrane permeability in day 50 organoids every 24 h, during 72 h of growth factor starvation. Quantification showed no changes in cell death as a result of GSK3 inhibition, either in baseline (0 h) or after 72 h of starvation (Figures 2I and 2J), indicating that chronic GSK3 inhibition has no impact on basal or starvation-mediated cell death, hence excluding reduced apoptosis as a plausible cause of the increased organoid size. Instead, quantification of the proliferation marker Ki67 showed a marked increase of actively dividing cells in organoids at day 18 (CTL 10 ± 0.7, CHIR 19 ± 1.3) (Figure 1H) and day 50 (CTL 4.3 ± 0.4, CHIR 8.0 ± 0.8) (Figure 1I) pointing to the regulation of progenitor proliferation as a core effect of GSK3 activity.

Transcriptional Regulation Associated to GSK3 Activity throughout Cortical Development

Abundant evidence supports an active role of GSK3 in neurogenesis (Hur and Zhou, 2010); however, since complete *GSK3* ablation causes systemic failure and early embryonic lethality (Hoeflich et al., 2000), its levels/activity are usually manipulated both *in vitro* and *in vivo* after the early stages of neurodevelopment have already been completed. The surprisingly mild effect of chronic GSK3 inhibition on neural maturation prompted us to dissect its role on gene expression by bulk RNA-seq at three critical time points recapitulating relevant stages of human cortical development (i.e., day 18: abundant apical radial glia; day 50: presence of intermediate progenitors and early neurons; and day 100: presence of lower layer neurons and beginning of astrogenesis) (Paşca et al., 2015).

A dissection of the most influential genes on component 1 of principal-component analysis identified genetic drivers of cell proliferation as main source of variability (Figures 3A and S3A) and highlighted the stronger impact of CHIR treatment at days 50 and 100. A survey of gene signatures defining specific stages of differentiation (active proliferation, early and late RGs, early and late neurons) (Figure S1) confirmed a sustained increase of the proliferation marker *MKI67* upon CHIR treatment at days 18 and 50 (Figure S1A–S1C), along with an upregulation in genes controlling distinct aspects of cell-cycle progression at days 50 and 100. Notably, we observed a robust upregulation of the anaphase promoting complex/cyclosome (APC/C), *CDC20* (Figures S1B and S1C), which has been implicated in the modulation of the synaptic connectivity regulator *NEUROD2* levels through the regulation of its ubiquitination (Yang et al., 2009). Intriguingly, despite the strong proliferation effect, the expression levels of canonical neuronal markers (*DCX*, *MEF2C*, *STMN2*) (Figures S1B and S1C), cortical layer makers (*POU3F2*, *CUX1*, *BCL11B*), and ventral fate determinants (*DLX1-2*, *ARX*, *GAD1-2*, *ASCL1*) (Figures S2A–S2C) showed either mild or no differences, whereas the neuron-specific microtubule-related genes showed differential modulation upon CHIR inhibition (i.e., upregulation of *TUBB3* and downregulation *MAP2*) (Figures S1B and S1C). Likewise, we observed a strong downregulation of *NEUROD2* expression at days 50 and 100 (Figures S1B and S1C), which could in turn explain the downregulation of several glutamate channel subunits observed at day 100 (Figures S1C and S1D).

To address the functional implications of chronic CHIR exposure, we performed stage-wise differential expression analysis (DEA) (Figures 3B–3D). DEA confirmed the strongest CHIR effect at day 50, with 898 differentially expressed

Figure 2. GSK3 Inhibition Disrupts Lumen Organization and Progenitor Proliferation Rate

(A) Experimental design: hPSCs differentiated following two parallel protocols, in 3D (up) cortical organoids or 2D (down) dual-smad inhibition. In both cases, parallel rounds were either exposed or not to GSK3 inhibitor CHI99021 (1 μM) starting from day 0 until the indicated sample collection time point.

(B) Representative captions from immunostaining performed for anti-Pals1(green)/Hoechst(blue), wide-field fluorescence images acquisition, 20×. Scale bar, 50 μm (zoom panel, 10 μm).

(C) Bar plots represent the average lumen number ± SD of five independent images for lines/conditions.

(D) Lumen area quantification was performed by CellProfiler software; unpaired t test; **p < 0.01, ***p < 0.001, ****p < 0.0001.

(E) Cell proliferation rate was estimated by CellTiter-Glo luminescence assay, with measurements every 24 h for 96 h in triplicate, three independent hPSC lines (n = 3).

(F) Representative bright-field captions of day 40 organoids. Scale bar, 500 μm.

(G) Growth curve performed in organoids differentiated for 40 days. Bright-field captions were taken at days 5, 9, 14, 20, 24, 30, 35, and 40. Points represent the average of 4 organoids per line. Size quantifications were performed with a custom-made FIJI function.

(H) Derivative of the growth-rate delta between time points. The delta was computed on the average of untreated or treated samples. SD was calculated as a cumulative SD across all replicates and samples from each condition of three independent hPSC lines (n), four organoids measured per line/time point (N) (N = 72, n = 3), unpaired t test; **p < 0.01, ****p < 0.0001.

(I) Representative images from day 50 organoids stained with CellTox green as a marker of cytotoxicity after 72 h of growth factor starvation (depletion B27 and growth factors). Scale bar, 200 μm.

(J) Quantification of CellTox fluorescence at 0, 24, 48, and 72 h after growth factor starvation.

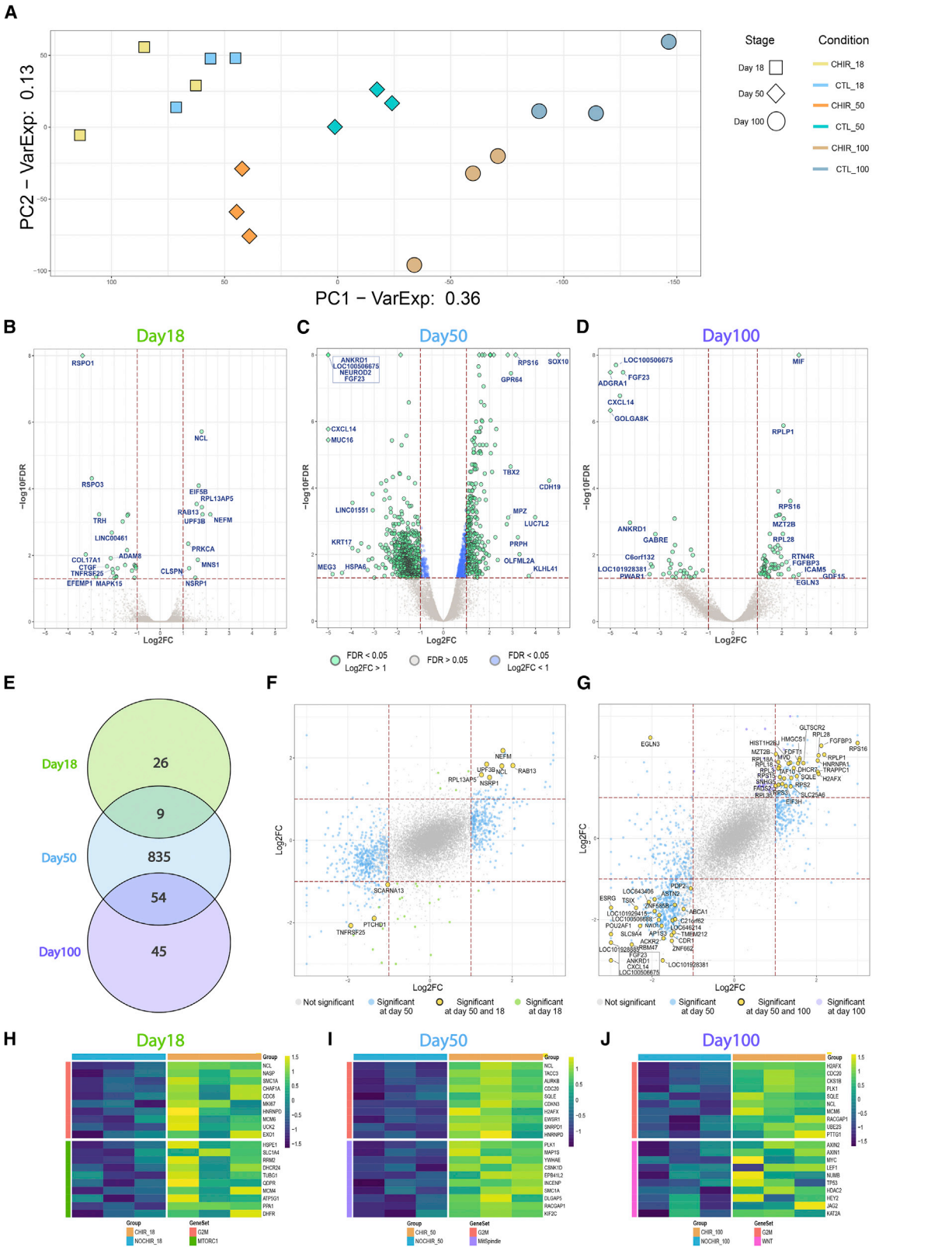

(legend on next page)

genes (DEGs) (Figure 3C) (full list of DEGs, Table S2). Ontology analysis revealed a persistent upregulation of categories linked to cell proliferation and DNA replication (nucleosome assembly) and a downregulation of cell surface components, as well as ion channels, including AMPA subunits (Figures S3C and S3D). While there were no DEGs preserved at all stages upon CHIR treatment, we identified 9 DEGs consistently dysregulated in the day 18 → day 50 transition and 54 DEGs in the day 50 → day 100 transition (Figure 3E). Interestingly, day 18 → day 50 shared DEGs included the upregulation of neurite outgrowth factors (*NEFM*, *NCL*, and *RAB13*), and downregulation of the brain morphogenesis modulator (*PTCHD1*) (Figure 3F), whereas the day 50 → day 100 dysregulation featured an abundant upregulation of protein translation and replication regulators (Figure 3G). The overall comparison of gene modulation across stages showed a stronger preservation in the fold changes trends between day 50 → day 100 (R = 0.62) compared with day 18 → day 50 (R = 0.45), despite the longer time span and increased cell-type diversity at later stages (Figures 3F and 3G), suggesting a more robust dependency of GSK3 activity occurring during this transition.

To gain deeper insight into the coordinated modulation of functionally related genes induced by GSK3 inhibition, we performed gene set enrichment analysis (GSEA). This approach confirmed a robust enrichment for pathways targeted by GSK3 activity (MTORC1, Myc signaling) and narrowed down the upregulation of G2-M transition modulators as a persistent feature of GSK3 transcriptional impact at all stages (Figures 3H–3J). Likewise, several of the identified GSEA categories (complete list in Table S3) are directly linked to the observed phenotypes, including the increased progenitor production (mammalian target of rapamycin complex 1 pathway), changes of cell polarity (mitotic spindle orientation) and neuronal fate (Wnt-β-catenin pathway). Interestingly, both gene ontology analysis at day 50 and GSEA (at all stages) point to the downregulation of inflammatory pathways by GSK3 inhibition, in line with a recognized role of GSK3 as mediator of neuroinflammation (Grimes and Jope, 2001b).

Cortical Organoids Recapitulate the Main Features of Mid-fetal Human Corticogenesis at the Single-Cell Level

Given the greater transcriptional impact of GSK3 observed at the day 50 → day 100 transition, we harnessed single-cell transcriptomics combined with distance-based analytical tools to break down the effects of CHIR exposure in terms of population frequencies and developmental trajectories found during this time frame. We carried out droplet-based single-cell mRNA-seq to profile over 30,000 cells (N = 33293) in 11 biological samples from unexposed and exposed cortical organoids at day 50 and day 100 of differentiation, attaining 15 unsupervised cell clusters defined using the Louvain modularity algorithm (Šubelj and Bajec, 2011). By projecting the expression levels of canonical population markers over uniform manifold approximation and projection (UMAP) (Figures 4A and 4B), combined with the overlap of cluster-specific genetic signatures from single-cell RNA-seq datasets of fetal human brain samples (Nowakowski et al., 2017) (Figure S4) and considering their position over diffusion map (Figure 4C), we grouped the Louvain clusters into five main population identities, including proliferating RG, IPCs (including a discernible subset of oRG), early neurons, neurons, and choroid. We then investigated the underlying developmental trajectories using a diffusion map algorithm (Coifman et al., 2005) (Figures 4C and 4D). This confirmed the presence of a hierarchical progression from RGs to postmitotic neurons linked by intermediate populations (Figure 4C). The application of pseudotime for lineage-branching reconstruction (Haghverdi et al.,

Figure 3. Impact of GSK3 Inhibition on the Transcriptional Landscape

(A) Principal component analysis performed on the whole transcriptome of untreated and CHIR-treated brain organoids at three stages of development: days 18, 50, and 100.

(B–D) Volcano plots illustrating the differential expression analysis for CHIR treatment at day 18 (B), day 50 (C), and day 100 (D). Results are reported for the pool of tested genes as $-\log_{10}$ false discovery rate (FDR) and $\log_2$ fold change (FC). Genes identified as significantly modulated (FDR < 5% and absolute $\log_2$FC > 1) are shown in green, while those respecting only the FDR threshold are depicted in blue and not significant genes (FDR > 5%) in gray. Gene symbols highlight the top 10 upregulated and downregulated genes (ranked by fold change) in each stage.

(E) Venn diagram depicting the overlap of modulated genes across developmental stages.

(F and G) Scatterplots representing the relationship of the fold change induced by GSK3 inhibition at day 50 on the x axis and day 18 on the y axis (F) or day 50 on the x axis and day 100 on the y axis (G), for the subset of genes tested in both conditions. DEGs shared between the two examined conditions are reported in yellow, while DEGs specific for days 18, 50, or 100 are in green, blue, or violet, respectively. Correlation coefficient calculated according the Spearman metrics––0.45 in (F) and 0.62 in (G).

(H–J) Gene expression profiles for selected gene sets significantly associated with CHIR treatment by GSEA: (H) day 18; (I) day 50; and (J) day 100. Expression levels (as *Z* score) for the top 10 ranking genes in the leading edge are visualized for each gene set. All analyses were done in three independent hPSC lines/time point (N = 18, n = 3).

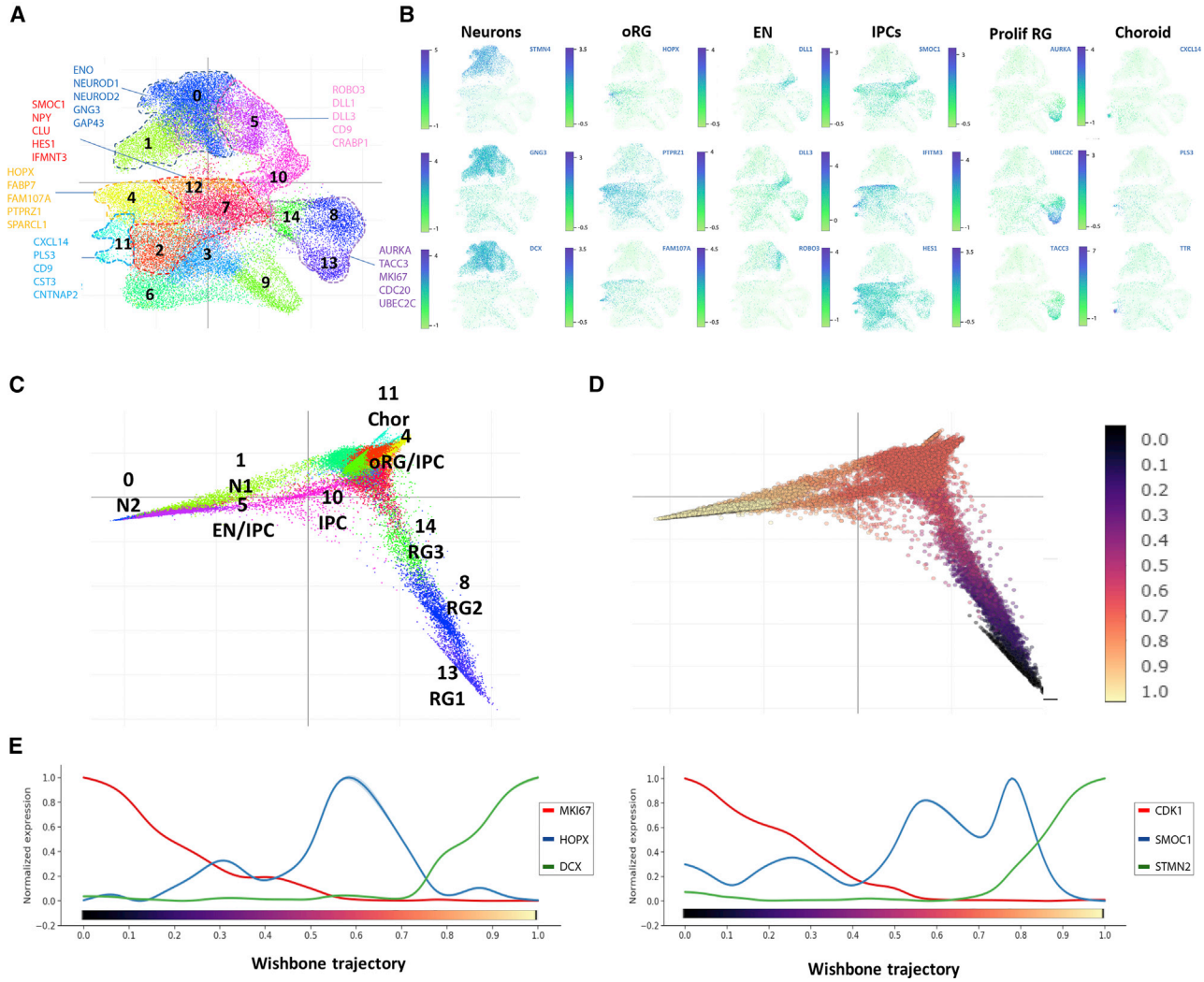

Figure 4. Cortical Organoids Recapitulate the Main Features of Cortical Development

(A) Louvain clusters in UMAP plot colored by cluster identity; lines depict population areas defined by contrast with markers obtained from human fetal brain dataset (radial glia, 8, 13, and 14; intermediate progenitor cells, 2, 7, and 12; outer radial glia, 4; early neurons, 5 and 10; neurons, 0 and 1; choroid 11).

(B) UMAP plots. For each sub-panel, cells (represented as dots) are colored according to the expression levels of representative cell-type markers: *STMN4*, *GNG3*, *DCX*, neurons; *HOPX*, *PTPRZ1*, *FAM107A*, outer radial glia; *DLL1*, *DLL3*, *ROBO3*, early neurons; *SMOC1*, *IFITM3*, *HES1*, intermediate progenitors; *AURKA*, *UBEC2C*, *TACC3*, proliferating progenitors; *CXCL14*, *PLS3*, *TTR*, choroid.

(C and D) Diffusion map representing the developmental trajectory of the system. Cells (dots) are colored according to cluster identity (C) and to pseudotime trajectory (D), from origin in black to terminal state in light yellow according to wishbone algorithm.

(E) Visualization of the expression levels of representative genes along pseudotime: *CDK1* and *MKI67*, proliferating progenitors; *DCX* and *STMN2*, neurons; *HOPX*, outer radial glia; *SMOC1*, intermediate progenitors. Analyses done in 33,293 cells from 6 hPSC lines from day 50 and 5 hPSC lines from day 100.

2016; Setty et al., 2016), with an origin anchored in the early progenitors, reproduced the organization of populations from RG to neurons (Figure 4D). Likewise, the distribution of expression of specific population markers confirmed the presence of a lineage path from RGs through the IPC-oRG transition and into early and late neural maturation stages (Figure 4E). Together, these results confirm that patterned cortical organoids recapitulate cardinal features of human corticogenesis, including the presence of early and intermediate progenitors, the emergence of oRGs and their hierarchical positioning in neurogenic trajectories.

GSK3 Inhibition Differentially Affects Specific Domains of Corticogenesis

A comparative analysis of subpopulations revealed a selective impact of GSK3 inhibition on the relative proportion of specific cell subtypes (Figures 5A–5H). A salient effect was the almost complete loss of a subpopulation characterized by the expression of genes expressed in choroid cells (*CXCL14*, *TPD52L1*, *PCP4*, *EMX2*) (Figures 5A and 5B), as well as a noticeable decrease in frequency (FQ) of *NEUROD2*-expressing cells at day 100 in neuronal clusters (0, 1, 5) without affecting *NEUROD6*- or *NEUROG2*-expressing cells (Figures 5C and 5D), underscoring the selectivity of GSK3 activity on these neurogenic pathways. It is worth noting that analysis of the frequency and distribution of cells expressing a canonical oRG gene signature (*HOPX*, *TNC*, *FAM107A*, *PTPRZ1*) (Pollen et al., 2015) (Figures 5E and 5F), showed a marked reduction in both frequency and expression levels upon CHIR treatment at day 100, which was further confirmed by a reduction of HOPX+ cells in the tissue (Figure 5I). Given the cardinal role of oRG on neuronal production and cortical expansion, we checked the distribution of expression of telencephalic markers, including forebrain determinant (*FOXG1*), early neurons (*DCX*), lower-layer (*BCL11B*, *RBFOX3*), and upper-layer (*SATB2*, *POU3F2*) markers. Whereas upper-layer markers were either not detected or present at very low frequencies, consistent with their surge at later stages of organoid corticogenesis, the expression of lower layer and general neuronal identity markers was unchanged by CHIR (Figure 5H), whereas *FOXG1* was significantly reduced at day 50 (Figures 5G and 5H). Interestingly, despite the mild changes frequency and expression levels of *BCL11B* at day 50 and day 100 (Figures 5H and S2), staining for its protein product (CTIP2)+ cells showed a drastic reduction in day 100 CHIR-treated organoids (Figure 5I), pointing to regulatory mechanisms at the post-transcriptional level reported to affect CTIP2 activity and stability (Selman et al., 2018; Zhang et al., 2012).

Next, to study the temporal associations between populations, we performed pseudotime analysis. The analysis of cell-type distribution across pseudotime uncovered a higher proportion of cells in both progenitor and mature areas upon chronic GSK3 inhibition at day 50 (Figure 6A). This result was compatible with two possibilities: (1) the cells identified as mature by predefined gene signatures could actually turn out to display mixed identities, co-expressing both progenitor and maturation markers as a result of a fundamental derangement of developmental hierarchies; or (2) the highly proliferative progenitors from CHIR-treated organoids undergo a faster transition through the intermediate stages or even skip them altogether. To test these hypotheses, we plotted proliferating/maturity signatures into UMAP and found no evidence of overlap in CHIR-treated organoids (Figure S5A); likewise, we did not observe an overlapping distribution between Ki67+ and DCX+ cells (Figure 1D), thus ruling out the possibility of a prevalent mixed identity. Instead, the contour plot (Figure 6A) pointed to a reduction in the intermediate populations in CHIR-treated organoids at days 50 and 100, consistent with the higher proportion of mature cells found at the same developmental stage (Figure 6A). Next, to further investigate the relations between populations, we used partition-based graph abstraction as a way to estimate the strength of connectivity across the cells belonging to each cluster, thus inferring transitional links among subpopulations. This approach confirmed a decrease of connections between intermediate progenitor clusters (yellow), including oRG, upon GSK3 inhibition, particularly evident at day 100 (Figure 6B), corroborating a CHIR-dependent overall reduction of the intermediate to maturity transition.

Finally, the application of pseudotime, independently to all conditions and stages, revealed two developmental trajectories, one that goes from RG to neurons through a subset of IPCs and one that becomes apparent by day 100 and ends in an oRG identity (Figure 6C). Strikingly, GSK3 inhibition resulted in a complete loss of the oRG-generating trajectory at day 100 (Figure 6C), an effect that could be reproduced bidirectionally by decomposing each trajectory into first and second components (Figure S5B). In agreement, *HOPX* distribution of expression on pseudotime peaked at day 100 in control organoids, while it remained stalled in day 100 CHIR-treated organoids (Figure 6C). Together, these results suggest that GSK3 inhibition results in a severe reduction of HOPX-expressing cells with the attending impact on oRG-dependent lineages.

DISCUSSION

This work provides the first dissection of the role of GSK3 activity throughout early to mid-fetal corticogenesis in a human background. Specifically, our integrated analysis of tissue and transcriptional regulation at single-cell resolution uncovers a key role for GSK3 activity in cortical tissue architecture, with a differential impact on neuronal output vis-a-vis a strong decrease of oRG production.

GSK3 activity has been implicated in the regulation of neocortical neuron production, with pronounced impact at late stages (Li et al., 2012), consistent with the increased transcriptional dysregulation that we observe in days 50 to 100 cortical organoids. Our in-depth transcriptional analysis indicates that not all aspects of cortical neurogenesis are equally affected, even in the face of the early increase in progenitor proliferation and massive morphologic disarray, which emphasizes the resilience and degree of

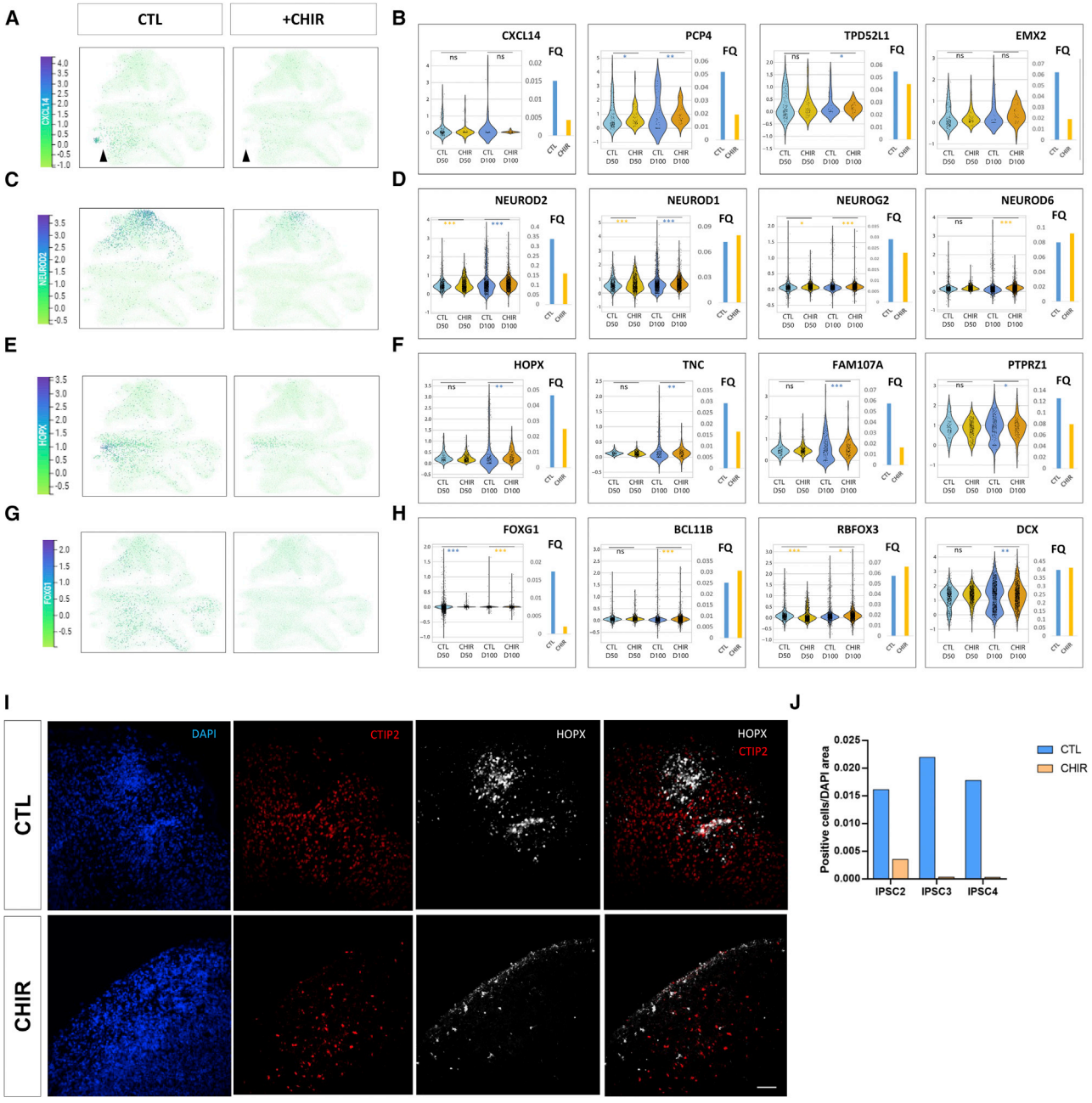

Figure 5. Effects of GSK3 Inhibition at a Single-Cell Level in Day 50 and 100 Cortical Organoids

(A–H) Visualization of normalized expression levels for genes identifying specific populations either in UMAP divided by CHIR-treated and control samples (A, C, E, and G). Sub-sampled cluster-specific expression levels (violin plots), Fisher test; ***$p < 0.001$, **$p < 0.01$, *$p < 0.05$. FQ, normalized cell frequencies of cells expressing detectable levels/total population (bar plots) (B, D, F, and H). The following genes are examined: (A and B) *CXCL14* in UMAP and *CXCL14*, *PCP4*, *TDP52L1*, *EMX2* in violin plots on cluster 11 for choroid population; (C and D) *NEUROD2* in UMAP and *NEUROD2*, *NEUROD1*, *NEUROG2*, and *NEUROD6* on clusters 0, 1, and 5 for neuronal markers; (E and F) *HOPX* in UMAP and *HOPX*, *TNC*, *FAM107A*, and *PTPRZ1* on cluster 4 for oRG markers; (G and H) *FOXG1* in UMAP and *FOXG1* (total) and *BCL11B*, *RBFOX3*, and *DCX* on clusters 0, 1, and 5 for dorsal telencephalon markers. Sub-sampling has been applied in order to randomly compare an equal number of cells for each category.

(I) Representative wide-field fluorescence images from day 100 organoids immunostained with anti-CTIP2 (red), anti-HOPX (gray), and DAPI (blue). Scale bar, 20 μm.

(J) Semiquantitative estimation of HOPX positive cells/DAPI area. Quantification corresponds to three organoids per line, three independent hPSC lines. Analyses done in 33,293 cells from 6 hPSC lines from day 50 and 5 hPSC lines from day 100.

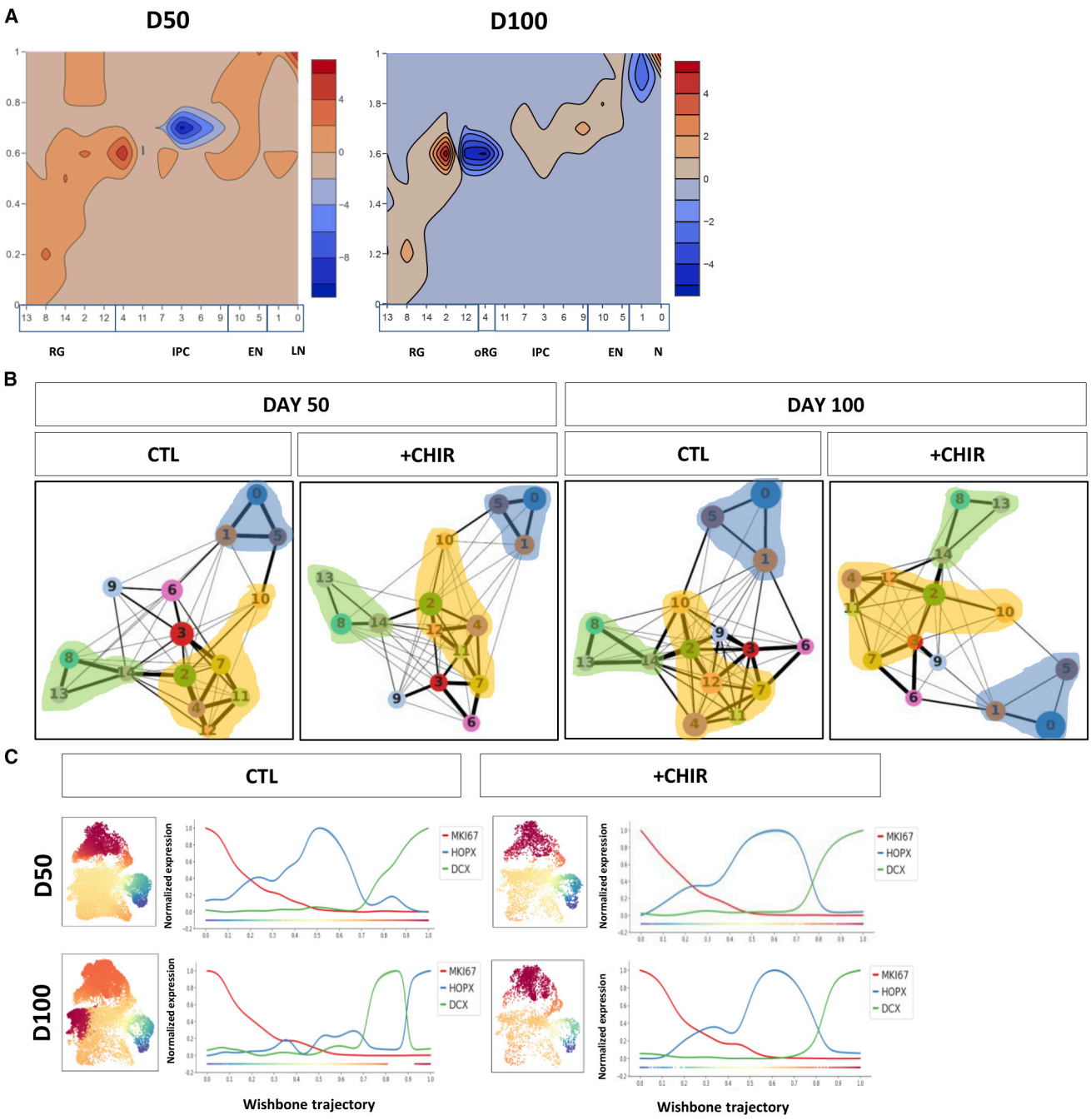

Figure 6. Effects of GSK3 Inhibition at a Single-Cell Level in Day 50 and Day 100 Cortical Organoids

(A) Contour plot representing the difference in frequency distribution in clusters and pseudotime intervals of treated versus untreated cells at days 50 and 100. Red depicts values higher in CHIR-treated cells, while blue depicts values higher in CTL-treated cells.

(B) Partition-based graph abstraction analysis applied stage- and treatment-wise on the 15 clusters identified on the complete dataset. Circle diameter represents the fraction of cells assigned to each cluster; edge thickness visualizes the strength of connections across cells of the related clusters. Shadows highlight areas: progenitors (green), neurons (blue), and intermediate progenitors (yellow).

(C) Over-imposition of pseudotime analyses performed separately for each experimental condition as a color scale on a UMAP calculated on the complete system. Blue (origin) and dark red (terminal state) according to wishbone trajectories. Visualization of the expression levels of representative genes along the condition-specific pseudotime. Analyses done in 33,293 cells from 6 hPSC lines from day 50 and 5 hPSC lines from day 100.

cell autonomy of the transcriptional programs involved in neuronal identity, even against the disruption of stereotypical tissue architecture. In particular, early neuronal driver *NEUROD2* was strongly downregulated in bulk transcriptomes and remained reduced both, in terms of expression levels and frequency in single cells, concomitantly with a reduced number of cells positive for low-layer markers TBR1 and CTIP2, while the frequency of cells expressing neurogenic drivers (*NEUROG2*), fetally expressed pan-neuronal markers (*DCX*, *STMN2*), and low-layer determinants (*RBFOX3*, *CUX1*) was either unchanged or only slightly differed in expression levels among very low cell frequencies. Interestingly, we found a decrease in *FOXG1* levels at day 18 bulk transcriptomes and in the frequency of *FOXG1*-expressing cells at day 50. These changes in *FOXG1* expression resulted in no evident posteriorizing effects, likely reflecting the minute fraction of *FOXG1*-positive cells at days 50 to 100 (consistently with its expression peaking at day 25; Birey et al., 2017) and the cortical organoid patterning that drives toward a telencephalic fate (Paşca et al., 2015). In light of the emerging disconnect between transcript and protein levels of several neurogenic transcription factors due to post-transcriptional regulation (Yoon et al., 2017), it will be interesting to determine the short- to long-term impact of such transcriptional alterations on the respective protein effectors.

Depletion of GSK3 activity using pharmacological inhibition or knockdown causes drastic changes in radial glial organization (Yokota et al., 2010). As polarization of radial glia is a prerequisite for cortical scaffolding, neuronal migration, and layering (Shah et al., 2017), its alterations result in impaired cortical plate formation (Beattie et al., 2017; Shah et al., 2017). The effects of GSK3 in radial glia organization constitute fast cellular responses triggered by phosphorylation of targets such as CRMP2, MAP1B, and CLASP, which in turn affects modifications and structural changes in microtubule cytoskeleton (Hur and Zhou, 2010; Yokota et al., 2010). We did not observe any differences in expression of canonical polarity markers or determinants of radial glia organization (data not shown); thus, in the human setting, the sustained morphological defects caused by GSK3 activity inhibition are not caused by transcriptional regulation of polarity determinants. Rather, the most salient transcriptional global effect was the upregulation of modulators of cell replication and, in particular, the G2M transition emerged as a recurrent target at all stages, indicating that the modulation of the G2M is a persistent feature of GSK3 activity throughout human corticogenesis.

During human corticogenesis, the bulk of neuronal production comes via IPCs that originate from RGs and are located in the subventricular zone (Bystron et al., 2008; Florio and Huttner, 2014). Spatiotemporal regulation of GSK3 activity is required for an appropriate transition from the proliferative to the neurogenic phase occurring during brain development (Kim et al., 2009). In our chronic setting, starting from a pluripotent state (day 0), GSK3 inhibition caused increased proliferation and polarity defects in NSCs, reflected also in larger organoid size. The dramatic increase in CHIR-dependent transcriptional dysregulation at day 50, compared with day 18, indicates that the early defects in NSCs are amplified in intermediate and committed progenitors, and suggests a higher reliance on GSK3 activity at later stages and stronger in IPCs. In agreement, the population breakdown by single-cell analysis revealed a decrease of IPCs and in particular oRGs.

Pseudotime trajectories showed that cortical organoids recapitulate the co-existence of a direct neurogenic trajectory, visible by day 50, that is juxtaposed to an indirect trajectory reaching an oRG identity by day 100, in agreement with a protracted wave of neurogenesis dependent on oRG production, known to be a salient feature of primate corticogenesis and responsible for lateral expansion of the human cortex (Bershteyn et al., 2017; Florio and Huttner, 2014). In sum, the disappearance of the indirect neurogenic trajectory at day 100 upon CHIR treatment points to a key role of GSK3 in the establishment of IPC/oRG populations. Our results thus indicate that, in humans, while GSK3 activity selectively contributes to different early RG-derived neuronal identities, it is pivotal for the later generation of oRG with the ensuing outcome in terms of oRG-dependent lineages.

EXPERIMENTAL PROCEDURES

hPSC Culture

Five different hPSC lines from different backgrounds (one ESC and four iPSCs) were used across all conducted experiments (relevant ethics approvals are referred to in the original publications reporting their first use and/or derivation). The culture conditions of hPSCs are described in Supplemental Experimental Procedures. Distribution of lines across experiments is delineated in Table S1.

Neural Induction in 2D and Lumen Quantification

Three biological replicates were analyzed for untreated and treated cells. From day 0 of neural induction, CHIR99021 was added to the medium at 1 μM concentration in parallel with neural induction with DMSO until day 20. At day 12, cells were moved to neural medium containing DMEM/F12 (Life Technologies) with N2 and B27 plus retinoic acid and 30 ng/mL brain-derived neurotrophic factor. Differentiation process and immunostaining procedure are described in Supplemental Experimental Procedures.

Proliferation Assay

Number of viable proliferating cells was estimated by luminescence assay CellTiter-Glo (Promega). In brief, 2×10^3 cells/well were plated in 96-well flat bottom plates (Corning) with 4

replicates per condition and left to proliferate for 96 h. Measurements were performed every 24 h. Each data point was normalized to a blank from unseeded wells.

Cortical Organoid Differentiation and Inhibition

Cortical organoids were differentiated as described previously (Paşca et al., 2015). A detailed protocol is given in Supplemental Experimental Procedures. Chronic GSK3 inhibition was performed by adding CHIR99021 (Merck SML1046) to the medium at day 0 (1 μM) and kept throughout the differentiation process until reaching the respective collection time points.

Growth Curve

Organoids were moved at day 0 to 96-well U-bottom ultra-low attachment plates (Corning) and kept individually to avoid fusions for image acquisition until day 12 of differentiation. From day 12 onward, organoids were moved individually to 24-well ultra-low attachment plates (Corning). Images were acquired with an EVOS Cell imaging System XL (Thermo) at the indicated differentiation days. Organoid size was calculated using an in-house developed custom-script (by C.E.V.) for FIJI software (v.1.49; NIH, USA).

Tissue Preservation and Staining

Organoids were fixed in 4% (vol/vol) paraformaldehyde for a minimum of 2 h for day 18 organoids to overnight for day 50 and day 100 organoids. Fixed organoids were washed twice with PBS and mounted on OCT cryopreservation medium on dry ice. Cryoblocks were preserved at −80°C until the moment of sectioning. Cryosections were prepared using Leica CM 1900 instrument with 5 μm thickness. Sections were incubated with 10 mM sodium citrate buffer (Normapur) for 45 min at 95°C + Tween 20 0.5% for simultaneous antigen retrieval and permeabilization. Antibody incubation details and image acquisition and quantification details are given in Supplemental Experimental Procedures.

Total RNA Extraction and Sequencing

Total RNA was isolated with the RNeasy Micro Kit (QIAGEN, Hilden, Germany) according to the manufacturer's instructions. RNA was quantified with Nanodrop and then the integrity was evaluated with Agilent 2100 Bioanalyzer. A TruSeq Stranded Total RNA LT Sample Prep Kit (Illumina) was used for library preparation starting from 500 ng of total RNA for each sample. Sequencing was performed with the Illumina NOVAseq 6000 platform, with an average depth of 35 million 50 bp paired-end reads per sample.

Bulk Transcriptome Analysis

Three biological replicates were analyzed for untreated and treated organoids at each time point, for a total of 18 samples subjected to bulk RNA-seq. The detailed analytical pipeline is described in Supplemental Experimental Procedures.

Single-Cell Suspension, cDNA Synthesis, Library Preparation, and Sequencing

Organoids were collected at days 50 or 100. Three to 5 organoids per condition were dissociated by incubation with a solution of 0.5 mg/mL trypsin + 0.22 mg/mL EDTA (Euroclone) with 10 μL of DNaseI 1,000 U/mL (Zymo Research) for 30–45 min according to organoid size. Digested suspensions were passed once through 0.4-μm Flowmi cell strainers, resuspended in PBS and counted using a TC20 automatic cell counter (Bio-Rad). Droplet-based single-cell partitioning and single-cell RNA-seq libraries were generated using the Chromium Single-Cell 3′ Reagent v2 Kit (10× Genomics, Pleasanton, CA) following the manufacturer's instructions. Detailed library preparation is given in Supplemental Experimental Procedures.

Single-Cell Transcriptome Analysis

Eleven biological samples (day 50, 3 untreated and 2 treated; day 100, 4 untreated and 2 treated) were examined by single-cell analysis, for a total of 33,293 cells and a median of 1,733 features for cells. Libraries from single-cell sequencing were aligned relying on the CellRanger v2.1 pipeline and using hg38 as reference. Array express accession number: E-MTAB-8337. Detailed single-cell transcriptome analysis is given in Supplemental Experimental Procedures.

Statistical Analysis

Statistical analyses were done using PRISM (GraphPad, version 6.0). Statistical significance was tested with the unpaired t test, considering each hPSC line as biological replicates (n) and total number of organoids per line (N). Treatments tested as variables. p values and significance, n and N are reported in each figure and legend. All results were expressed as means ± SD. No data points were excluded from the reported analyses.

ACCESSION NUMBERS

The accession number for the bulk RNA seq reported in this paper is ArrayExpress: E-MTAB-8325. The accession number for the single-cell RNA seq reported in this paper is ArrayExpress: E-MTAB-8337.

SUPPLEMENTAL INFORMATION

Supplemental Information can be found online at https://doi.org/10.1016/j.stemcr.2019.09.005.

AUTHOR CONTRIBUTIONS

A.L.-T., S.T., N.C., M.L., and B.M.C. organoid differentiation and sample collection for the different experiments. C.E.V. and C.C. bioinformatic analysis. A.L.-T., S.T., and N.C. single-cell experimental procedures. A.L.-T. and M.L. organoid growth curve. A.L.-T., N.C., S.T., and P.L.R. stainings, quantifications, and statistical analysis. P.C., R.I., and E.C. neural induction experiments in 2D. M.T.R. proliferation assay in 2D. E.T. and F.T. cortical organoid generation and library preparation. M.D.S., I.L.-N., G.M., and M.P. contributed with funding and expertise. A.L.-T. wrote the manuscript with contributions from all authors. G.T. conceived, designed, and supervised the study.

ACKNOWLEDGMENTS

This work was supported by the Associazione Italiana per la Ricerca sul Cancro (AIRC) (IG 2014-2018 to G.T.); EPIGEN Flagship Project

of the Italian National Research Council (CNR) (to G.T., G.M., and M.P.); the European Research Council (ERC DISEASEAVATARS no. 616441 to G.T.); Fondazione Cariplo (2017-0886 to A.L.-T.); EDC-MixRisk, European Union's Horizon 2020 research and innovation programme (Grant No 634880. to G.T., C.C., and N.C.); END-poiNTs, European Union's Horizon 2020 research and innovation programme (Grant No 825759. to G.T. and C.C.); European Commission H2020 Project Joint Programme – Neurodegenerative Disease Research (JPND) ModelPolyQ (Grant No 643417" to R.I., P.C., and E.C.); Fondazione Italiana per la Ricerca sul Cancro (FIRC) and Fondazione Istituto Europeo di Oncologia - Centro Cardiologico Monzino (IEO-CCM) (to P.L.R.); the AIRC grant no. IG2016-ID18575 (to M.P.) and the ERC Consolidator grant no. 617978 (to M.P.) and the IEO Single Cell Program. S.T. and N.C. are PhD students within the European School of Molecular Medicine (SEMM). M.P. is a founder, shareholder and a member of the scientific advisory board of CheckmAb s.r.l. We are grateful to Pierre-Luc Germain for providing scripts that facilitated the analysis, to Andreas Püschel (University of Münster, Germany) for critical comments on the introduction, to Stefano Piccolo (University of Padua, Italy) for sharing of expertise, and to Federica Pisati from the tissue processing facility and the IEO genomic unit team.

Received: March 4, 2019
Revised: September 12, 2019
Accepted: September 13, 2019
Published: October 10, 2019

REFERENCES

Aberle, H., Bauer, A., Stappert, J., Kispert, A., and Kemler, R. (1997). β-Catenin is a target for the ubiquitin-proteasome pathway. EMBO J. *16*, 3797–3804.

Amiri, A., Coppola, G., Scuderi, S., Wu, F., Roychowdhury, T., Liu, F., Pochareddy, S., Shin, Y., Safi, A., Song, L., et al. (2018). Transcriptome and epigenome landscape of human cortical development modeled in organoids. Science *362*, eaat6720.

Beattie, R., Postiglione, M.P., Burnett, L.E., Laukoter, S., Streicher, C., Pauler, F.M., Xiao, G., Klezovitch, O., Vasioukhin, V., Ghashghaei, T.H., et al. (2017). Mosaic analysis with double markers reveals distinct sequential functions of Lgl1 in neural stem cells. Neuron *94*, 517–533.e3.

Bershteyn, M., Nowakowski, T.J., Pollen, A.A., Di Lullo, E., Nene, A., Wynshaw-Boris, A., and Kriegstein, A.R. (2017). Human iPSC-derived cerebral organoids model cellular features of lissencephaly and reveal prolonged mitosis of outer radial glia. Cell Stem Cell *20*, 435–449.e4.

Betizeau, M., Cortay, V., Patti, D., Pfister, S., Gautier, E., Bellemin-Ménard, A., Afanassieff, M., Huissoud, C., Douglas, R.J., Kennedy, H., et al. (2013). Precursor diversity and complexity of lineage relationships in the outer subventricular zone of the primate. Neuron *80*, 442–457.

Birey, F., Andersen, J., Makinson, C.D., Islam, S., Wei, W., Huber, N., Fan, H.C., Metzler, K.R.C., Panagiotakos, G., Thom, N., et al. (2017). Assembly of functionally integrated human forebrain spheroids. Nature *545*, 54–59.

Bystron, I., Blakemore, C., and Rakic, P. (2008). Development of the human cerebral cortex: Boulder Committee revisited. Nat. Rev. Neurosci. *9*, 110–122.

Camp, J.G., Badsha, F., Florio, M., Kanton, S., Gerber, T., Wilsch-Bräuninger, M., Lewitus, E., Sykes, A., Hevers, W., Lancaster, M., et al. (2015). Human cerebral organoids recapitulate gene expression programs of fetal neocortex development. Proc. Natl. Acad. Sci. U S A *112*, 15672–15677.

Coifman, R.R., Lafon, S., Lee, A.B., Maggioni, M., Nadler, B., Warner, F., and Zucker, S.W. (2005). Geometric diffusions as a tool for harmonic analysis and structure definition of data: multiscale methods. Proc. Natl. Acad. Sci. U S A *102*, 7432–7437.

Conforti, P., Besusso, D., Bocchi, V.D., Faedo, A., Cesana, E., Rossetti, G., Ranzani, V., Svendsen, C.N., Thompson, L.M., Toselli, M., et al. (2018). Faulty neuronal determination and cell polarization are reverted by modulating HD early phenotypes. Proc. Natl. Acad. Sci. U S A *115*, E762–E771.

Eiraku, M., Watanabe, K., Matsuo-Takasaki, M., Kawada, M., Yonemura, S., Matsumura, M., Wataya, T., Nishiyama, A., Muguruma, K., and Sasai, Y. (2008). Self-organized formation of polarized cortical tissues from ESCs and its active manipulation by extrinsic signals. Cell Stem Cell *3*, 519–532.

Florio, M., and Huttner, W.B. (2014). Neural progenitors, neurogenesis and the evolution of the neocortex. Development *141*, 2182–2194.

Fumoto, K., Lee, P.C., Saya, H., and Kikuchi, A. (2008). AIP regulates stability of Aurora-A at early mitotic phase coordinately with GSK-3β. Oncogene *27*, 4478–4487.

Grimes, C.A., and Jope, R.S. (2001a). Creb DNA binding activity is inhibited by glycogen synthase kinase-3?? and facilitated by lithium. J. Neurochem. *78*, 1219–1232.

Grimes, C.A., and Jope, R.S. (2001b). The multifaceted roles of glycogen synthase kinase 3β in cellular signaling. Prog. Neurobiol. *65*, 391–426.

Haghverdi, L., Büttner, M., Wolf, F.A., Buettner, F., and Theis, F.J. (2016). Diffusion pseudotime robustly reconstructs lineage branching. Nat. Methods *13*, 845–848.

Hoeflich, K.P., Luo, J., Rubie, E.A., Tsao, M.S., Jin, O., and Woodgett, J.R. (2000). Requirement for glycogen synthase kinase-3β in cell survival and NF-κB activation. Nature *406*, 86–90.

Hur, E.M., and Zhou, F.Q. (2010). GSK3 signalling in neural development. Nat. Rev. Neurosci. *11*, 539–551.

Johansson, P.A., Cappello, S., and Götz, M. (2010). Stem cells niches during development—lessons from the cerebral cortex. Curr. Opin. Neurobiol. *20*, 400–407.

Kadoshima, T., Sakaguchi, H., Nakano, T., Soen, M., Ando, S., Eiraku, M., and Sasai, Y. (2013). Self-organization of axial polarity, inside-out layer pattern, and species-specific progenitor dynamics in human ES cell-derived neocortex. Proc. Natl. Acad. Sci. U S A *110*, 20284–20289.

Kim, W.Y., Wang, X., Wu, Y., Doble, B.W., Patel, S., Woodgett, J.R., and Snider, W.D. (2009). GSK-3 is a master regulator of neural progenitor homeostasis. Nat. Neurosci. *12*, 1390–1397.

Lancaster, M.A., Renner, M., Martin, C.A., Wenzel, D., Bicknell, L.S., Hurles, M.E., Homfray, T., Penninger, J.M., Jackson, A.P., and

Knoblich, J.A. (2013). Cerebral organoids model human brain development and microcephaly. Nature *501*, 373–379.

Li, S., Mattar, P., Zinyk, D., Singh, K., Chaturvedi, C.-P., Kovach, C., Dixit, R., Kurrasch, D.M., Ma, Y.-C., Chan, J.A., et al. (2012). GSK3 temporally regulates neurogenin 2 proneural activity in the neocortex. J. Neurosci. *32*, 7791–7805.

Di Lullo, E., and Kriegstein, A.R. (2017). The use of brain organoids to investigate neural development and disease. Nat. Rev. Neurosci. *18*, 573–584.

Ma, Y., Wang, X., Chen, J., Li, B., Hur, E.-M., and Saijilafu. (2017). Differential roles of glycogen synthase kinase 3 subtypes alpha and beta in cortical development. Front. Mol. Neurosci. *10*, 391.

Ma, Y.C., Song, M.R., Park, J.P., Henry Ho, H.Y., Hu, L., Kurtev, M.V., Zieg, J., Ma, Q., Pfaff, S.L., and Greenberg, M.E. (2008). Regulation of motor neuron specification by phosphorylation of neurogenin 2. Neuron *58*, 65–77.

Mariani, J., Vittoria, M., Palejev, D., Tomasini, L., Coppola, G., Szekely, A.M., Horvath, T.L., and Vaccarino, M.V. (2012). Modeling human cortical development in vitro using induced pluripotent stem cells. Proc. Natl. Acad. Sci. U S A *109*, 12770–12775.

Mariani, J., Coppola, G., Zhang, P., Abyzov, A., Provini, L., Tomasini, L., Amenduni, M., Szekely, A., Palejev, D., Wilson, M., et al. (2015). FOXG1-dependent dysregulation of GABA/glutamate neuron differentiation in autism spectrum disorders. Cell *162*, 375–390.

McCubrey, J.A., Rakus, D., Gizak, A., Steelman, L.S., Abrams, S.L., Lertpiriyapong, K., Fitzgerald, T.L., Yang, L.V., Montalto, G., Cervello, M., et al. (2016). Effects of mutations in Wnt/β-catenin, hedgehog, Notch and PI3K pathways on GSK-3 activity—diverse effects on cell growth, metabolism and cancer. Biochim. Biophys. Acta *1863*, 2942–2976.

Nowakowski, T.J., Bhaduri, A., Pollen, A.A., Alvarado, B., Mostajo-Radji, M.A., Di Lullo, E., Haeussler, M., Sandoval-Espinosa, C., Liu, S.J., Velmeshev, D., et al. (2017). Spatiotemporal gene expression trajectories reveal developmental hierarchies of the human cortex. Science *358*, 1318–1323.

Paşca, A.M., Sloan, S.A., Clarke, L.E., Tian, Y., Makinson, C.D., Huber, N., Kim, C.H., Park, J.-Y., O'Rourke, N.A., Nguyen, K.D., et al. (2015). Functional cortical neurons and astrocytes from human pluripotent stem cells in 3D culture. Nat. Methods *12*, 671–678.

Patsch, C., Challet-Meylan, L., Thoma, E.C., Urich, E., Heckel, T., O'Sullivan, J.F., Grainger, S.J., Kapp, F.G., Sun, L., Christensen, K., et al. (2015). Generation of vascular endothelial and smooth muscle cells from human pluripotent stem cells. Nat. Cell Biol. *17*, 994–1003.

Pollen, A.A., Nowakowski, T.J., Chen, J., Retallack, H., Sandoval-Espinosa, C., Nicholas, C.R., Shuga, J., Liu, S.J., Oldham, M.C., Diaz, A., et al. (2015). Molecular identity of human outer radial glia during cortical development. Cell *163*, 55–67.

Qian, X., Nguyen, H.N., Song, M.M., Hadiono, C., Ogden, S.C., Hammack, C., Yao, B., Hamersky, G.R., Jacob, F., Zhong, C., et al. (2016). Brain-region-specific organoids using mini-bioreactors for modeling ZIKV exposure. Cell *165*, 1238–1254.

Quadrato, G., Nguyen, T., Macosko, E.Z., Sherwood, J.L., Yang, S.M., Berger, D.R., Maria, N., Scholvin, J., Goldman, M., Kinney, J.P., et al. (2017). Cell diversity and network dynamics in photosensitive human brain organoids. Nature *545*, 48–53.

Selman, W.H., Esfandiari, E., and Filtz, T.M. (2018). Alteration of Bcl11b upon stimulation of both the MAP kinase- and Gsk3-dependent signaling pathways in double-negative thymocytes. Biochem. Cell Biol. *97*, 201–213.

Setty, M., Tadmor, M.D., Reich-Zeliger, S., Angel, O., Salame, T.M., Kathail, P., Choi, K., Bendall, S., Friedman, N., and Pe'Er, D. (2016). Wishbone identifies bifurcating developmental trajectories from single-cell data. Nat. Biotechnol. *34*, 637–645.

Shah, B., Lutter, D., Tsytsyura, Y., Glyvuk, N., Sakakibara, A., Klingauf, J., and Püschel, A.W. (2017). Rap1 GTPases are master regulators of neural cell polarity in the developing neocortex. Cereb. Cortex *27*, 1253–1269.

Šubelj, L., and Bajec, M. (2011). Unfolding communities in large complex networks: combining defensive and offensive label propagation for core extraction. Phys. Rev. E Stat. Nonlin. Soft Matter Phys. *83*. https://doi.org/10.1103/PhysRevE.83.036103.

Taverna, E., Götz, M., and Huttner, W.B. (2014). The cell biology of neurogenesis: toward an understanding of the development and evolution of the neocortex. Annu. Rev. Cell Dev. Biol. *30*, 465–502.

Watanabe, K., Kamiya, D., Nishiyama, A., Katayama, T., Nozaki, S., Kawasaki, H., Watanabe, Y., Mizuseki, K., and Sasai, Y. (2005). Directed differentiation of telencephalic precursors from embryonic stem cells. Nat. Neurosci. *8*, 288–296.

Yang, Y., Kim, A.H., Yamada, T., Wu, B., Bilimoria, P.M., Ikeuchi, Y., De La Iglesia, N., Shen, J., and Bonni, A. (2009). A Cdc20-APC ubiquitin signaling pathway regulates presynaptic differentiation. Science *326*, 575–578.

Yokota, Y., Eom, T.-Y., Stanco, A., Kim, W.-Y., Rao, S., Snider, W.D., and Anton, E.S. (2010). Cdc42 and Gsk3 modulate the dynamics of radial glial growth, inter-radial glial interactions and polarity in the developing cerebral cortex. Development *137*, 4101–4110.

Yoon, K.J., Ringeling, F.R., Vissers, C., Jacob, F., Pokrass, M., Jimenez-Cyrus, D., Su, Y., Kim, N.S., Zhu, Y., Zheng, L., et al. (2017). Temporal control of mammalian cortical neurogenesis by m6A methylation. Cell *171*, 877–889.e17.

Zhang, L.J., Vogel, W.K., Liu, X., Topark-Ngarm, A., Arbogast, B.L., Maier, C.S., Filtz, T.M., and Leid, M. (2012). Coordinated regulation of transcription factor bcl11b activity in thymocytes by the mitogen-activated protein kinase (MAPK) pathways and protein sumoylation. J. Biol. Chem. *287*, 26971–26988.

Stem Cell Reports, Volume *13*

Supplemental Information

Human Cortical Organoids Expose a Differential Function of GSK3 on Cortical Neurogenesis

Alejandro López-Tobón, Carlo Emanuele Villa, Cristina Cheroni, Sebastiano Trattaro, Nicolò Caporale, Paola Conforti, Raffaele Iennaco, Maria Lachgar, Marco Tullio Rigoli, Berta Marcó de la Cruz, Pietro Lo Riso, Erika Tenderini, Flavia Troglio, Marco De Simone, Isabel Liste-Noya, Giuseppe Macino, Massimiliano Pagani, Elena Cattaneo, and Giuseppe Testa

Supplemental information

1. Supplemental figures S1 to S5 legends
2. Supplemental experimental procedures
3. References related to experimental procedures
4. Supplemental tables. List of differentially expressed genes. List of GSEA categories (Excel files).

1. Supplemental figure legends

Figure S1. Expression profiles for gene signatures defining specific developmental stages. Related to Figure 3. Stripcharts for expression levels (in log2cpm) from bulk RNA sequencing at day 18 (A), day 50 (B) and day 100 (C). Unexposed samples are visualized in turquoise, CHIR-exposed samples in orange. Blue and red boxes highlight respectively genes down- or up-regulated by CHIR treatment, considering the following thresholds from RNASeq bulk differential expression analysis: *: nominal p-value < 0.05; **: nominal p-value < 0.01; ***: FDR < 0.05 and absolute $\log_2$FC > 1.

Figure S2. Expression profiles for genes related to dorsalising/ventralizing fate. Stripcharts for expression levels (in log2cpm) from bulk RNA sequencing at day 18 (A), day 50 (B) and day 100 (C). Unexposed samples are visualized in turquoise, CHIR-exposed samples in orange. Blue and red boxes highlight respectively genes down- or up-regulated by CHIR treatment, considering the following thresholds from RNASeq bulk differential expression analysis: *: nominal p-value < 0.05; **: nominal p-value < 0.01.

Figure S3. Breakdown of stage-wise differential expression analysis. Related to Figure 3. A. Top-100 genes according to absolute loading value for the first component from Principal Component Analysis. **B.** Results of gene ontology enrichment analysis performed for Biological Process GO domain on the 100 genes selected as detailed in A; p-values for the top-10 categories are shown. **C**. Gene expression profiles (as z-scores) for the genes identified in bulk RNASeq as modulated by GSK3 treatment (FDR < 0.05, absolute $\log_2$FC > 1) at day 18 (A), day 50 (B) and day 100 (C). **D**. Results of gene ontology enrichment analysis performed on the DEGs identified at day 50, divided for up-regulated and down-regulated genes. Bar plots depict the p-values for the top-10 Cellular Component GO terms.

Figure S4. Overlap of Louvain clusters to cell identities within human fetal data single cell transcriptomes. Related to Figure 4. A. For each sub-panel, cells (represented as dots) are colored according to the expression levels of paired combinations of representative cell type markers (DCX, STMN2 = mature neurons), (ENO2, ST18 = early neural progenitors), (FAM107A, HOPX = outer radial glia), (SMOC1, S100B = intermediate progenitors) (CDK1, CDC20, MKI67 = proliferating progenitors) (CXCL14 = choroid/Astro). **B.** Heatmap of the overlaps between marker genes characterizing the internal organoids clusters and external gene signatures of the relevant single cell clusters from human fetal brains (Nowakowski et al., 2017). Colors are based on the log2Enrichment computed for each pair of comparisons. * indicates an overlap with p-value < 0.05.

Figure S5. UMAP plots for proliferation/maturity distribution and pseudotime decomposition. Related to Figure 6. A. Visualization of expression levels of proliferation/progenitor markers (in red: CDK1, MKI67) coupled with maturity markers (in green: DCX, STMN2), (in yellow: overlapping expression). UMAPS are visualized separately for each timepoint and condition. **B.** First and second components inferred from condition-wise diffusion components and visualized as color gradient on UMAP. The two extremes of the color scale (origin-blue and dark red-outcome) represent the distance in the relative diffusion component. CTL D100 is the only condition with an end point in oRG area.

2. Supplemental experimental procedures

hPSC culture. hPSC lines were cultured under feeder-free conditions on Matrigel (BD Biosciences) coated dishes (diluted 1:40 matrigel:DMEM/F12) and grown in Tesr™ E8™ medium (Stem Cell Technologies). Cells were passaged upon treatment with ReLeSR (Stem Cell Technologies). All differentiation procedures were performed on iPSC lines with at least 15 passages after reprogramming. Pluripotent lines came from different individuals representing either human iPSC or ESC lines previously described (Adamo et al., 2015; González et al., 2014). All the cultures were regularly tested and maintained mycoplasma free.

Table 1. Distribution of hPSC lines used in this study.

Experiment/Line	809-1-5 (iPSC1)	KOLF2CL (iPSC2)	MIFF1-3 (iPSC3)	3391B (iPSC4)	HUES8 (ESC)
ICC		X	X	X	X
Rosette formation assay		X	X	X	

Growth curve			X	X	X
Bulk RNAseq	X	X	X	X	X
Single cell RNAseq	X	X	X	X	X

Neural induction and lumen quantification. hPSC cells were plated at a density of 0.7×10^5 cells cm^2 on Matrigel (BD Biosciences) coated dishes in grow medium supplemented with 10 µM ROCK inhibitor (Y-2763221, Cell Guidance System). Cell cultures were expanded for two days until they were 70% confluent. The starting differentiation medium includes DMEM/F12 (Life Technologies) with N2 and B27 without retinoic acid (Life Technologies), supplemented with 500 nM LDN193189 (Sigma) and 10 µM SB431542 (Tocris). Cells were fixed at day 20 in 4% (wt/vol) paraformaldehyde (PFA) for 15 minutes at room temperature (RT) and washed 3 times with phosphate-buffered saline (PBS). Cells were then permeabilized with PBS containing 0.5% Triton X-100 (Sigma) and blocked with 10% (vol/vol) normal goat serum (NGS; Vector) for 1 hour at RT. Next, cells were incubated overnight at 4°C. The following primary antibodies and dilutions were used: Anti-PALS1, (Proteintech 117710-1-AP). Object identification module of Cell Profiler software (v.2.1.1) was used to automatically quantify lumens (number and size of Pals1 positive areas) of neural rosettes.

Cortical organoid protocol. hPSCs were plated onto cell cycle-arrested mouse embryonic feeders (MEFs)(Millipore) for one passage, colonies grown for at least 48h and then enzymatically detached by incubation with 0.7 mg/ml dispase (Invitrogen: 17105-041) for approx. 30 min. Suspended colonies were subsequently transferred into ultra-low-attachment 100 mm plastic plates (Corning) in FGF2-free knockout serum medium. For the first 24 h (day 0), the medium was supplemented with the ROCK inhibitor Y-27632 (EMD Chemicals). For neural induction, dorsomorphin (Merck, 5 µM) and SB-431542 (Tocris, 10 µM) were added to the medium until day 5. From day 6 onward, organoids were moved to neural medium (NM) containing Neurobasal (Invitrogen 10888), B-27 serum substitute without vitamin A (Invitrogen 12587), GlutaMax 1:100 (Fisher 35050071), 100 U/ml penicillin and streptomycin (Invitrogen) and 50 mM b-Mercaptoethanol (Gibco 31350010). The NM was supplemented with 20 ng/ml FGF2 (Thermo) and 20 ng/ml EGF (Tocris) for 19 days with daily medium change in the first 10 days, and every other day for the subsequent 9 days. On day 12, floating organoids were moved to orbital shaker (VWR Standard Orbital Shaker, Model 1000) and kept on constant shaking at 50 rpm to promote nutrient and oxygen exchange. To induce neurogenesis, FGF2 and EGF were replaced with 20 ng/ml BDNF (Peprotech) and 20 ng/ml NT3 (Peprotech) starting at day 25, while from day 43 onwards only NM without growth factors was used for medium changes every other day.

Primary and secondary antibodies used and quantifications. Primary antibodies were prepared in PBS + 5% normal donkey serum (Jackson Immuno Resarch) overnight at 4°C. The following primary antibodies and dilutions were used: anti-PAX6, 1:200 (Biolegend PRB-278B); anti-KI67, 1:200 (Abcam ab15580); anti-NESTIN, 1:500 (Millipore MAB5326); anti–DCX, 1:1000 (BD Biosciences 611706); anti-TBR1, 1:200 (Abcam ab31940), anti-HOPX, 1:50 (Sigma-Aldrich HPA030180), Anti CTIP2 1:200 (Abcam ab18465). After primary incubation, sections were washed three times with PBS and the incubated with appropriate secondary antibodies: anti-rabbit Alexa 488-conjugated (Bethyl A090-516D2) anti-mouse, Alexa 594-conjugated (Bethyl A110-305B4) (Molecular Probes, Invitrogen) diluted 1:500 in blocking solution and incubated for 2 h at RT. Before mounting, sections were incubated with Hoechst 33258 (5 µg/mL; Molecular Probes, Invitrogen) or DAPI 1:5000 (Merck), as indicated on each caption. Quantification of nuclear markers was done by using the automatic cluster counter ITCN plugin from FIJI (v.1.49 NIH-USA) for at least 3 organoids from 3 independent lines. Images were RGB converted and cluster counts were done over pre-defined concentric grids from VLS. The relative number of positive cells was calculated as a percentage of total DAPI+ cells. Images were acquired with a Leica DMI 6000B microscope (10x, 20x and 40x objectives) and analyzed with LAS-AF imaging software and then processed using Image J (v1.49 NIH, USA) to adjust contrast for optimal RGB rendering. Semi-quantitative measurements were made in imageJ, the background noise was removed with a sliding paraboloid filter of dimension 500 px, then a gaussian filter was applied. A positive cell was considered the local maxima with a minimum threshold of signal to noise. To evaluate the density of cells we consider organoid slice stained with DAPI, from the images of the whole organoid we remove, with a sliding paraboloid filter, the background and then apply a common threshold on all the conditions. The area of the resulting mask is considered as area occupied by nuclei and used as normalization.

Bulk transcriptome analysis. *Differential gene expression.* Gene expression quantification at the gene level was performed by Salmon (version 0.8.2) (Patro et al., 2017), using hg38 RefSeq annotation. To estimate differential expression, the matrix of gene counts was analyzed by edgeR (version 3.20.9) (Robinson et al., 2009). For each time point, genes with an expression level of at least 2 cpm (count per million) in at least 3 samples were selected for the analysis. Small genes, ribosomal genes and fusion genes were excluded. After TMM normalization, differential expression analysis comparing treated to untreated samples was performed using a likelihood ratio test on the coefficients of a negative binomial model. Significantly modulated genes were selected setting an absolute value of log2 fold change (Log2FC) higher than 1 and a false discovery rate (FDR) lower than 5%. Log2 cpm values, were

used for heatmap representation of gene expression profiles (visualized as z-scores). Heatmaps were produced with pheatmap R package (version 1.0.10, Raivo Kolde (2018). pheatmap: Pretty Heatmaps.). Analyses were performed in R version 3.4.4. Functional annotation of biological functions was performed by Gene ontology analysis and Gene set enrichment analysis (GSEA) using as set source H1 collection from the Molecular Signature Database (Liberzon et al., 2015). *Gene Ontology Enrichment Analysis.* Gene ontology enrichment analysis for the Cellular Component domain of the ontology was performed on the 898 DEGs identified at day 50, split in up-regulated and down-regulated genes. The pool of tested genes (as selected for differential expression analysis) was used as background. The analysis was performed by topGO (version 2.30.1) (Adrian Alexa and Jorg Rahnenfuhrer 2016). topGO: Enrichment Analysis for Gene Ontology), relying on Fisher test and Weight01 method to take into account ontology hierarchy; minimum node size was set at 15. After imposing an enrichment cut-off of 2, a 0.01 p-value cut off was applied to select significantly enriched GO terms. Barplot in supplementary figure 4 shows the top-10 categories ranked for p-value.

Gene set enrichment analysis. GSEA was applied to each developmental stage with GSAA software, version 1.2 (Xiong et al., 2014). Raw reads for the same genes tested for differential expression were analyzed by GSAASeqSP (permutation type 'gene set').

Single cell library preparation and sequencing. Briefly, a small volume (6 - 8 µl) of single-cell suspension at a density of 1000 cells/µl was mixed with RT-PCR master mix and immediately loaded together with Single-Cell 3′ gel beads and partitioning oil into a single-cell 3′ Chip. The gel beads were coated with unique primers bearing 10× cell barcodes, unique molecular identifiers (UMI) and poly(dT) sequences. The chip was then loaded onto a Chromium instrument (10× Genomics) for single-cell GEM generation and barcoding. RNA transcripts from single cells were reverse-transcribed within droplets to generate barcoded full-length cDNA using Clontech SMART technology. After emulsion disruption, cDNA molecules from one sample were pooled and preamplified. Finally, amplified cDNAs were fragmented, and adapter and sample indices were incorporated into finished libraries which were compatible with Illumina sequencing. The final libraries were quantified by Qubit system (Thermo) and calibrated with an in-house control sequencing library. The size profiles of the pre-amplified cDNA and sequencing libraries were examined by Agilent Bioanalyzer 2100 using a High Sensitivity DNA chip (Agilent). Two indexed libraries were equimolarly pooled and sequenced on Illumina NOVAseq 6000 platform using the v2 Kit (Illumina, San Diego, CA) with a customized paired-end, dual indexing format according to the recommendation by 10× Genomics. Using proper cluster

density, a coverage around 250 M reads per sample (2000–5000 cells) were obtained corresponding to at least 50,000 reads/cell.

Single cell transcriptome analysis. Before downstream analyses, data deriving from the 11 samples was integrated by Seurat v3.0-alpha analytical framework (Stuart et al., 2018). After normalization, anchors for data integration were identified considering 3000 anchor points (genes) and 40 dimensions. For data reduction, UMAP was applied with 50 nearest neighbors (nn); cluster initial positions were set considering PAGA node position (Scanpy v1.3.1) (Wolf et al., 2018). On the integrated dataset, clusters were identified by applying Louvain with Multilevel Refinement from Seurat with resolution parameter at 0.7. This resulted in the identification of 15 clusters. For cluster annotation, we applied the FindMarker Seurat function, using MAST as test and filtering for up-regulated genes with adjusted P value < 0.05. The obtained lists were compared in an overlap analysis with gene lists derived from two published single cell datasets: from the WGCNA analysis of single cell clusters of human fetal brains (paper by Nowakowski et al, DOI: 10.1126/science.aap8809), data were downloaded from the web portal at https://cells.ucsc.edu/?ds=cortex-dev and upregulated genes (vg_diff.float>1.5) were selected for each relevant cluster, from the differential expression analysis of single nuclei clusters (Table S6 of the paper by Amiri et al, DOI: 10.1126/science.aat6720), upregulated genes (fold change > 0 and adjusted P value < 0.05) were selected for each relevant cluster. P values and enrichment coefficients were computed relative to a universe of 3000 genes used for all the other single cell analysis. Cluster-specific expression levels of biologically-relevant genes identified among the top dysregulated were visualized by violin plots, stratified for stage and treatment. To test for unbalance in the number of highly expressing cells for representative genes per cluster or cluster set, a threshold of expression at the 90th percentile was fixed, and the number of cells above or below the threshold in treated and untreated cells was compared by Fisher test. The identification of the threshold and sub-sequent analysis was performed on the sub-sampled dataset, separately for Day 50 and Day 100.
Cell cycle analysis were performed using Scanpy function score_genes_cell_cycle, relying on the genes from (Kowalczyk et al., 2015). Diffusion map algorithm for dimensionality reduction was performed with Scanpy with 50 nn. Pseudotime analysis for lineage branching reconstruction was applied using wishbone algorithm (Setty et al., 2016). The analysis was performed on the complete dataset, as well as separately for each of the four biological conditions in order to infer stage or treatment-selective trajectories; the origin was identified with the same method applied on complete dataset. Trajectories were reproduced defining using at least 3 different markers. Partition-based

graph abstraction (PAGA) algorithm was applied on the complete dataset, as well as separately for each of the four biological conditions and plotted with layout Reingold Tilford. The position of the nodes identified on the complete dataset was exploited in the graph for each biological condition.

3. References related to experimental procedures

Adamo, A., Atashpaz, S., Germain, P.-L., Zanella, M., D'Agostino, G., Albertin, V., Chenoweth, J., Micale, L., Fusco, C., Unger, C., et al. (2015). 7q11.23 dosage-dependent dysregulation in human pluripotent stem cells affects transcriptional programs in disease-relevant lineages TL - 47. Nat. Genet. *47 VN-r*, 132–141.

González, F., Zhu, Z., Shi, Z.D., Lelli, K., Verma, N., Li, Q. V., and Huangfu, D. (2014). An iCRISPR platform for rapid, multiplexable, and inducible genome editing in human pluripotent stem cells. Cell Stem Cell.

Kowalczyk, M.S., Tirosh, I., Heckl, D., Rao, T.N., Dixit, A., Haas, B.J., Schneider, R.K., Wagers, A.J., Ebert, B.L., and Regev, A. (2015). Single-cell RNA-seq reveals changes in cell cycle and differentiation programs upon aging of hematopoietic stem cells. Genome Res.

Liberzon, A., Birger, C., Thorvaldsdóttir, H., Ghandi, M., Mesirov, J.P., and Tamayo, P. (2015). The Molecular Signatures Database Hallmark Gene Set Collection. Cell Syst.

Nowakowski, T.J., Bhaduri, A., Pollen, A.A., Alvarado, B., Mostajo-Radji, M.A., Di Lullo, E., Haeussler, M., Sandoval-Espinosa, C., Liu, S.J., Velmeshev, D., et al. (2017). Spatiotemporal gene expression trajectories reveal developmental hierarchies of the human cortex. Science (80-.).

Patro, R., Duggal, G., Love, M.I., Irizarry, R.A., and Kingsford, C. (2017). Salmon provides fast and bias-aware quantification of transcript expression. Nat. Methods.

Robinson, M.D., McCarthy, D.J., and Smyth, G.K. (2009). edgeR: A Bioconductor package for differential expression analysis of digital gene expression data. Bioinformatics.

Setty, M., Tadmor, M.D., Reich-Zeliger, S., Angel, O., Salame, T.M., Kathail, P., Choi, K., Bendall, S., Friedman, N., and Pe'Er, D. (2016). Wishbone identifies bifurcating developmental trajectories from single-cell data. Nat. Biotechnol.

Wolf, F.A., Angerer, P., and Theis, F.J. (2018). SCANPY: Large-scale single-cell gene expression data analysis. Genome Biol.

4. Supplemental tables.

Table 2. List of differentially expressed genes.

Table 3. List of GSEA categories (Excel files).

Figure S1.

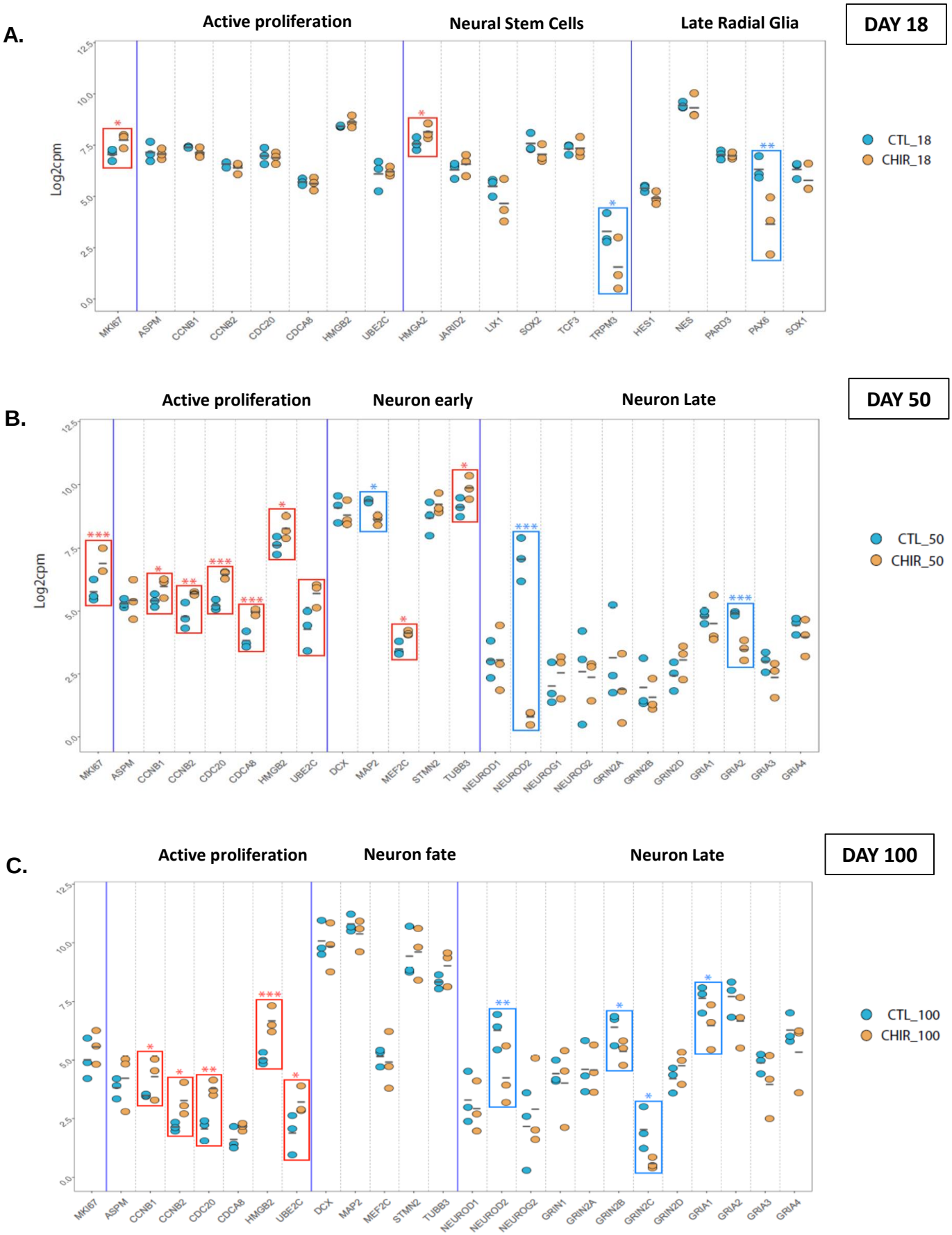
A.
Active proliferation
Neural Stem Cells
Late Radial Glia
DAY 18
Log2cpm
MKI67
ASPM
CCNB1
CCNB2
CDC20
CDCA8
HMGB2
UBE2C
HMGA2
JARID2
LIX1
SOX2
TCF3
TRPM3
HES1
NES
PARD3
PAX6
SOX1
CTL_18
CHIR_18
B.
Active proliferation
Neuron early
Neuron Late
DAY 50
Log2cpm
DCX
MAP2
MEF2C
STMN2
TUBB3
NEUROD1
NEUROD2
NEUROG1
NEUROG2
GRIN2A
GRIN2B
GRIN2D
GRIA1
GRIA2
GRIA3
GRIA4
CTL_50
CHIR_50
C.
Active proliferation
Neuron fate
Neuron Late
DAY 100
GRIN1
GRIN2C
CTL_100
CHIR_100

Figure S2.

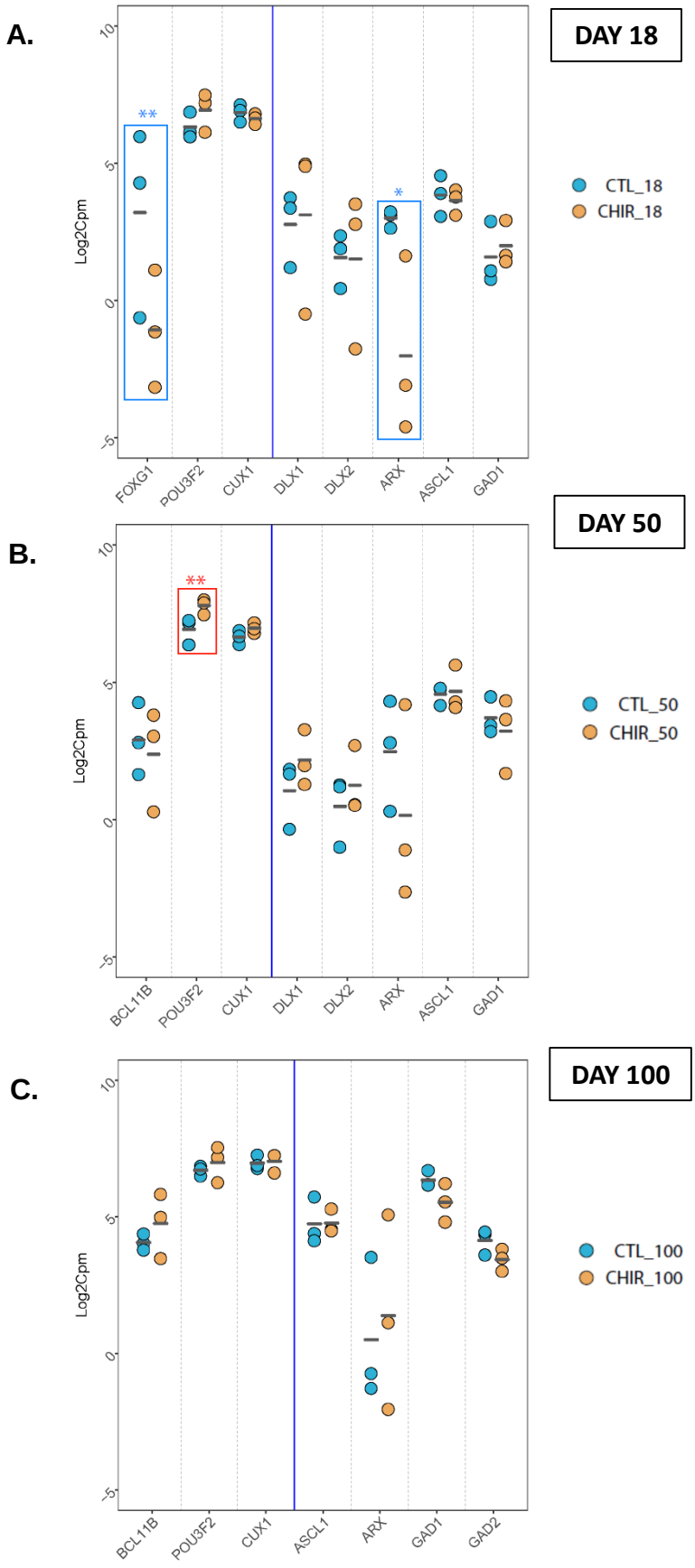
A.
DAY 18
Log2Cpm
10
5
0
-5
**
*
FOXG1
POU3F2
CUX1
DLX1
DLX2
ARX
ASCL1
GAD1
CTL_18
CHIR_18
B.
DAY 50
Log2Cpm
**
BCL11B
POU3F2
CUX1
DLX1
DLX2
ARX
ASCL1
GAD1
CTL_50
CHIR_50
C.
DAY 100
Log2Cpm
BCL11B
POU3F2
CUX1
ASCL1
ARX
GAD1
GAD2
CTL_100
CHIR_100

Figure S3.

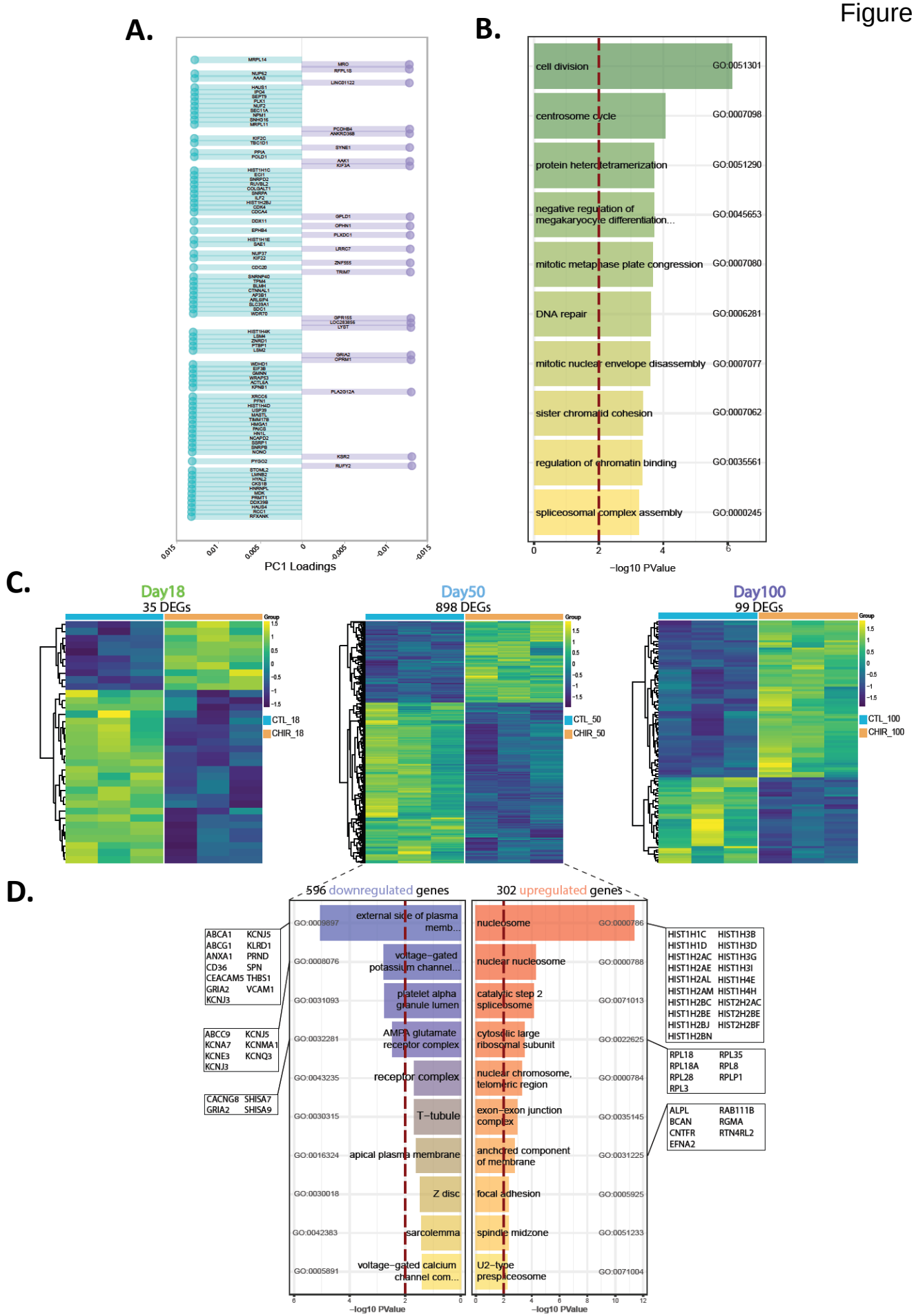
A.
PC1 Loadings
B.
cell division GO:0051301
centrosome cycle GO:0007098
protein heterotetramerization GO:0051290
negative regulation of megakaryocyte differentiation... GO:0045653
mitotic metaphase plate congression GO:0007080
DNA repair GO:0006281
mitotic nuclear envelope disassembly GO:0007077
sister chromatid cohesion GO:0007062
regulation of chromatin binding GO:0035561
spliceosomal complex assembly GO:0000245
−log10 PValue
C.
Day18
35 DEGs
CTL_18
CHIR_18
Day50
898 DEGs
CTL_50
CHIR_50
Day100
99 DEGs
CTL_100
CHIR_100
D.
596 downregulated genes
302 upregulated genes
GO:0009897 external side of plasma memb...
GO:0008076 voltage−gated potassium channel...
GO:0031093 platelet alpha granule lumen
GO:0032281 AMPA glutamate receptor complex
GO:0043235 receptor complex
GO:0030315 T−tubule
GO:0016324 apical plasma membrane
GO:0030018 Z disc
GO:0042383 sarcolemma
GO:0005891 voltage−gated calcium channel com...
ABCA1 KCNJ5
ABCG1 KLRD1
ANXA1 PRND
CD36 SPN
CEACAM5 THBS1
GRIA2 VCAM1
KCNJ3
ABCC9 KCNJ5
KCNA7 KCNMA1
KCNE3 KCNQ3
KCNJ3
CACNG8 SHISA7
GRIA2 SHISA9
−log10 PValue
GO:0000786 nucleosome
GO:0000788 nuclear nucleosome
GO:0071013 catalytic step 2 spliceosome
GO:0022625 cytosolic large ribosomal subunit
GO:0000784 nuclear chromosome, telomeric region
GO:0035145 exon−exon junction complex
GO:0031225 anchored component of membrane
GO:0005925 focal adhesion
GO:0051233 spindle midzone
GO:0071004 U2−type prespliceosome
HIST1H1C HIST1H3B
HIST1H1D HIST1H3D
HIST1H2AC HIST1H3G
HIST1H2AE HIST1H3I
HIST1H2AL HIST1H4E
HIST1H2AM HIST1H4H
HIST1H2BC HIST2H2AC
HIST1H2BE HIST2H2BE
HIST1H2BJ HIST2H2BF
HIST1H2BN
RPL18 RPL35
RPL18A RPL8
RPL28 RPLP1
RPL3
ALPL RAB11B
BCAN RGMA
CNTFR RTN4RL2
EFNA2
−log10 PValue

Figure S4.

A

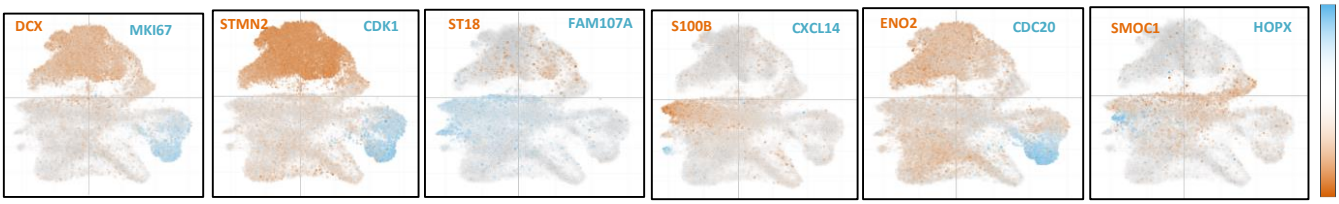
DCX
MKI67
STMN2
CDK1
ST18
FAM107A
S100B
CXCL14
ENO2
CDC20
SMOC1
HOPX

B

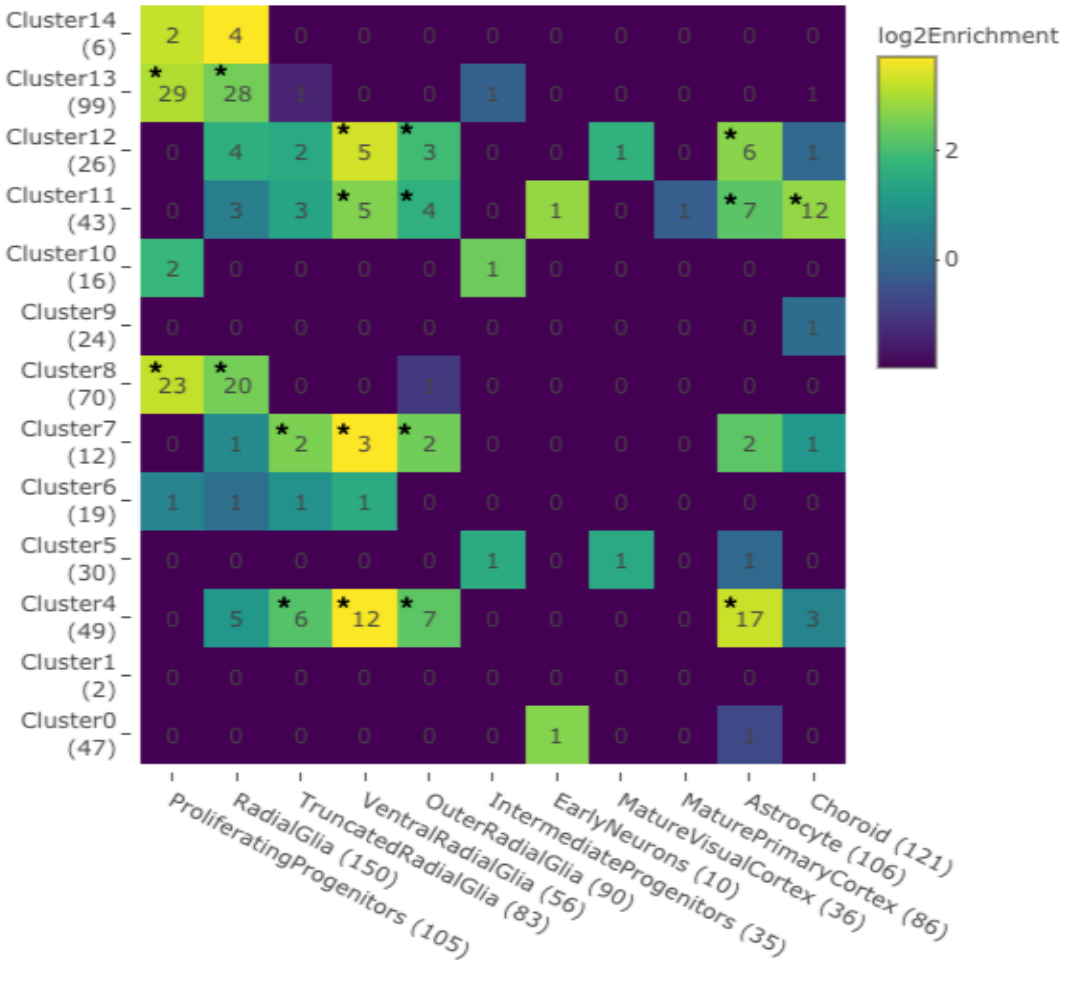
Cluster14 (6)
Cluster13 (99)
Cluster12 (26)
Cluster11 (43)
Cluster10 (16)
Cluster9 (24)
Cluster8 (70)
Cluster7 (12)
Cluster6 (19)
Cluster5 (30)
Cluster4 (49)
Cluster1 (2)
Cluster0 (47)
ProliferatingProgenitors (105)
RadialGlia (150)
TruncatedRadialGlia (83)
VentralRadialGlia (56)
OuterRadialGlia (90)
IntermediateProgenitors (35)
EarlyNeurons (10)
MatureVisualCortex (36)
MaturePrimaryCortex (86)
Astrocyte (106)
Choroid (121)
log2Enrichment
2
0

Figure S5.

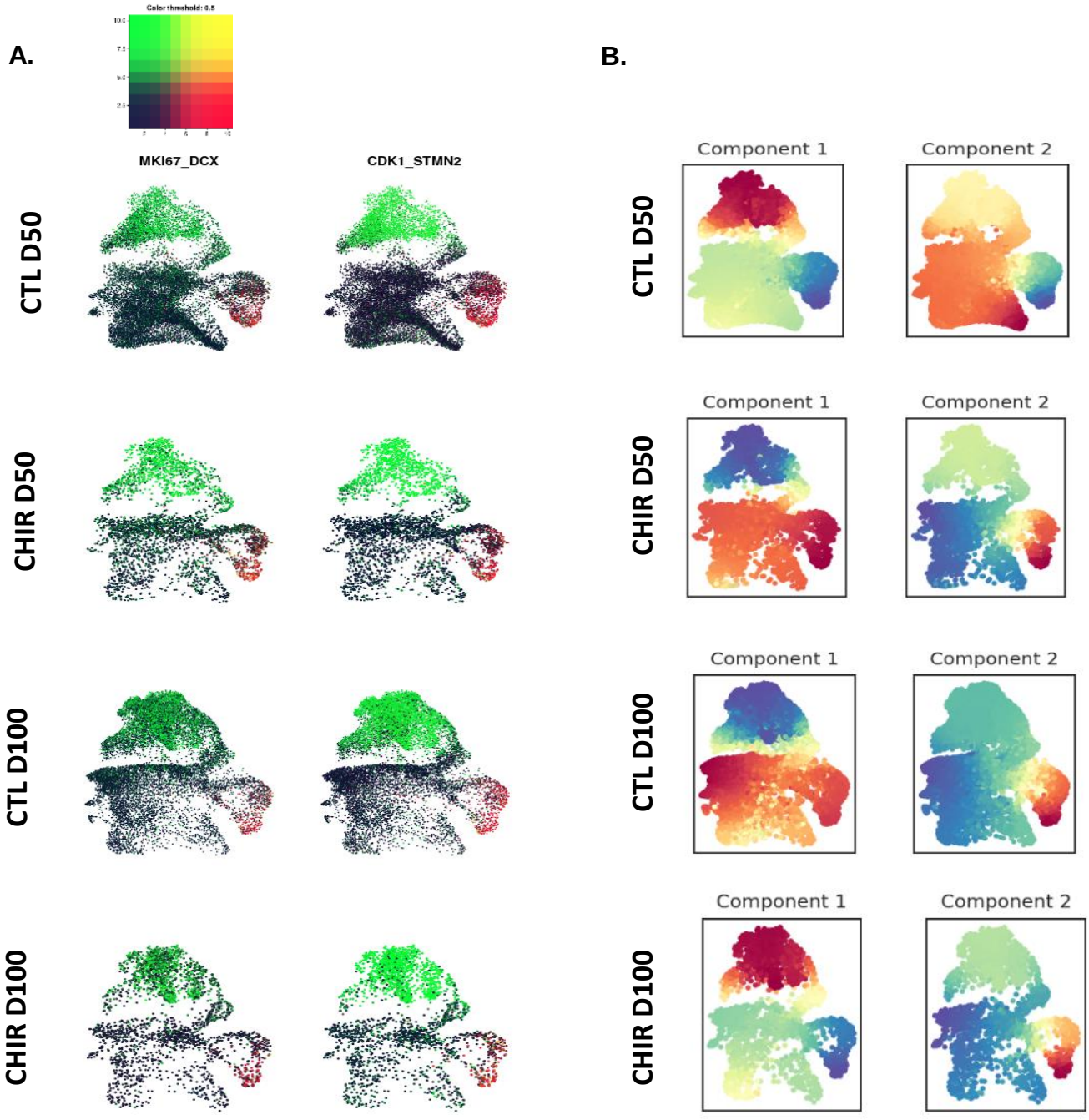
A.
Color threshold: 0.5
MKI67_DCX
CDK1_STMN2
CTL D50
CHIR D50
CTL D100
CHIR D100
B.
Component 1
Component 2
CTL D50
CHIR D50
CTL D100
CHIR D100